NAWI Graz
Natural Sciences

TU Graz

Jennifer Prohinig, BSc

Influence of Pt-H defects on Si p^+/n diode characteristics

MASTER'S THESIS

to achieve the university degree of

Diplom-Ingenieur

Master's degree programme: Advanced Materials Science

submitted to

Graz University of Technology

Supervisor:

Univ.-Prof. Ph.D. Peter Hadley
Institute of Solid State Physics

Graz, October 2018

Deutsche Fassung:
Beschluss der Curricula-Kommission für Bachelor-, Master- und Diplomstudien vom 10.11.2008
Genehmigung des Senates am 1.12.2008

EIDESSTATTLICHE ERKLÄRUNG

Ich erkläre an Eides statt, dass ich die vorliegende Arbeit selbstständig verfasst, andere als die angegebenen Quellen/Hilfsmittel nicht benutzt, und die den benutzten Quellen wörtlich und inhaltlich entnommenen Stellen als solche kenntlich gemacht habe.

Graz, am …………………………… ………………………………………………..
(Unterschrift)

Englische Fassung:

STATUTORY DECLARATION

I declare that I have authored this thesis independently, that I have not used other than the declared sources / resources, and that I have explicitly marked all material which has been quoted either literally or by content from the used sources.

…………………………… ………………………………………………..
date (signature)

Abstract

The insertion of platinum (Pt) in silicon (Si) diodes is a widely spread technique to control the minority carrier lifetime and therefore influence the device switching behaviour. If such diodes are exposed to hydrogen during some processing steps, the formation of Pt-H complexes may occur. In this thesis the influence of Pt-H related defects on Si diode performance is discussed. Standard characterization techniques such as high voltage current voltage (HV-IV) and capacitance voltage (CV) measurements combined with deep-level transient spectroscopy (DLTS) for defect identification are utilized. A defect level close to Si mid-bandgap ($E_C - 0.50$ eV) was assigned to Pt-H and it is shown that it increases the diode leakage current in reverse and the non-ideality factor in forward operation. It was found that crystal lattice damage such as vacancies caused by proton implantation tends to bind hydrogen to form, for instance shallow hydrogen-related donors, which may reduce the concentration of Pt-H defects throughout the whole device. Furthermore it is shown that annealing at temperatures larger than 600 K leads to a dissociation of the Pt-H defect level and thus a significant reduction in diode leakage current governed by carrier generation. Modelling this dissociation assuming a first order reaction an activation energy of 1.4 eV is obtained.

This thesis resulted from a cooperation with KAI - Kompetenzzentrum Automobil- und Industrieelektronik GmbH and Infineon Technologies Austria AG. The main results were presented at the International Semiconductor Conference CAS 2018.

Zusammenfassung

Das Einbringen von Platin (Pt) in Silzium (Si) Dioden ist eine weit verbreitete Technik um die Minoritätsladungsträgerlebensdauer und damit das Schaltverhalten des Bauteils zu beeinflussen. Werden solche Dioden während eines Prozesschrittes Wasserstoff ausgesetzt, kann es zur Bildung von Pt-H Komplexen kommen. In dieser Arbeit wird die Auswirkung von Pt-H Komplexen auf das Leistungsverhalten von Si Dioden untersucht.
Es werden Standard-Charakterisierungsmethoden wie Strom-Spannungs- (IV) und Kapazitäts-Spannungs- (CV) Messungen in Kombination mit *Deep-Level Transient Spectroscopy* (DLTS) benutzt. Ein Defektlevel nahe der Mitte der Si Bandlücke ($E_C - 0.50$ eV) wurde Pt-H zugeordnet und es konnte gezeigt werden, dass dieser Defekt sowohl den Leckstrom in Sperrrichtung, als auch den non-ideality Faktor in Vorwärtsrichtung erhöht. Es wurde festgestellt, dass durch Protonenimplantation entstandene Schäden im Kristallgitter, wie zum Beispiel Leerstellen, bevorzugt Wasserstoff an sich binden, was zu einer reduzierten Pt-H Konzentration im gesamten Bauteil zur Folge haben kann. Des Weiteren wird gezeigt, dass Tempern bei Temperaturen höher als 600 K zur Dissoziation des Pt-H Levels und somit einer erheblichen Reduktion des Leckstroms führen. Durch Modellierung des Dissoziationsprozesses unter Annahme einer Reaktion erster Ordnung wurde eine Aktivierungsenergie von 1.4 eV berechnet.

Diese Arbeit wurde in Kooperation mit der KAI - Kompetenzzentrum Automobil- und Industrieelekronik GmbH und der Infineon Technologies Austria AG realisiert. Die wichtigsten Ergebnisse dieser Arbeit wurden auf der Internationalen Halbleiterkonferenz CAS 2018 präsentiert.

Acknowledgement

I would like to express my gratitude to:

My supervisor at KAI Kompetenzzentrum Automobil- und Industrieelektronik Fabian Rasinger for his great explanations, patience and constant support with my thesis.

Gregor Pobegen for having me in his team and giving me the chance to further develop my skills at a non-university research institution.

Prof. Peter Hadley for supervising my thesis from TU Graz.

This work was funded by the Austrian Research Promotion Agency (FFG, Project No. 863947).

Contents

Abstract ii

Zusammenfassung iii

1 Introduction 1

2 Physical basics 3

3 Platinum deep levels in silicon 6

4 Experimental techniques 7

4.1 Deep-Level Transient Spectroscopy (DLTS) 7
4.1.1 Measurement principle 7
4.1.2 Steady-state reverse bias 8
4.1.3 Filling of the traps 8
4.1.4 Electron emission 9
4.1.5 Capacitance transients 10
4.1.6 DLTS analysis 11
4.1.7 Influence of measurement parameters on the DLTS spectrum 14
4.1.8 Minority Carrier Transient Spectroscopy (MCTS) 17
4.1.9 Current Transient Spectroscopy (IDLTS) 17
4.1.10 Constant-capacitance DLTS (CCDLTS) 18
4.1.11 Depth profiling with DLTS 19
4.2 Capacitance-voltage (CV) measurements 19
4.3 Current-voltage (IV) measurements 20
4.4 Spreading Resistance Profiling (SRP) 22
4.5 Isothermal annealing 24

5 Measurement instrumentation 27

5.1 Cryogenic probe station 27

5.2 Waferbow measurement station . . . 28

6 Investigated samples **30**

7 Experimental results **32**

7.1 Motivation . . . 32
7.2 Diode characteristics in forward and reverse operation . . . 33
7.3 High-voltage CV measurements . . . 34
7.4 Separation of leakage current components . . . 35
7.5 Defect identification with DLTS . . . 36
7.6 Calculation of defect profiles from reverse IV measurement . . . 39
7.7 SRP results . . . 41
7.8 DLTS depth profiles . . . 43
7.9 Annealing experiments . . . 44
7.9.1 DLTS spectra after annealing . . . 45
7.9.2 Influence on reverse current . . . 46
7.9.3 Determination of dissociation energy . . . 48
7.10 Connection between trap concentration and derivative of reverse current . . . 53

8 Conclusion and Outlook **54**

List of Symbols **vi**

List of Tables **viii**

List of Figures **x**

Bibliography **xiv**

1 Introduction

Platinum (Pt) is introduced on purpose in today's silicon power diodes. Pt atoms occupying substitutional sites in the Si lattice create two discrete levels within the Si band gap: an acceptor level 0.23 eV below the conduction band and a donor level 0.32 eV above the valence band [15]. Pt therefore acts as an efficient minority carrier lifetime killer while, at the same time, it is not causing detrimental high leakage currents [2]. The reduced carrier lifetime has a large influence on the device performance by decreasing the reverse recovery charge and thus allowing for very high switching frequencies while keeping switching losses low.
Another wide-spread application for tailoring electrical properties of high power devices is proton implantation [12]. The lattice damage induced in Si by the implanted protons is used to form shallow hydrogen-related donor complexes. These donor complexes are electrically activated after an additional annealing step at elevated temperature. Since the penetration depth of the protons can be adjusted by the implantation energy, layers of higher doping density are formed which are acting as a field-stop [23] in these power devices. By doing so the device is able to withstand higher reverse voltages before avalanche breakdown at a certain thickness.
However, there is a strong interaction between transition metals (TM) such as Pt and hydrogen, thus the electrical properties of TM centres can be greatly modified [13]. It is also known that the hydrogenation of substitutional TM centres can shift the impurity level position [27] but can in some cases also lead to complete passivation of the defect [25]. Thus the electrical properties of such TM-H complexes are of high interest.

In this thesis the influence of Pt-H complexes on the Si diode characteristics is investigated. The samples examined are industrially processed high voltage p^+/n diodes with Pt doping implanted for lifetime control. There are two different types of samples: the ones have an additional field-stop implanted from the backside using protons the other ones have not. Apart from that, all the diodes underwent the exact same processing steps. An enhancement of Pt-H formation in the diodes with proton field-stop is expected.
The experimental methods used in this thesis are high voltage current-voltage (IV), capacitance-voltage (CV) measurements and spreading-resistance profiling (SRP). Furthermore the focus is

put on the investigation of Pt related defects utilizing deep-level transient spectroscopy (DLTS). The density of defect states, their energetic position within band gap as well as their impact on device performance are determined. Additionally, isothermal annealing experiments are performed. The aim of this thesis is to gain a better understanding of the interaction between substitutional Pt for lifetime control and additional proton implantation and the influence of Pt-H complexes, assumed to be formed as a consequence, on the diode characteristic in forward and reverse operation. Finally, annealing experiments are performed to check the thermal stability of assumed Pt-H complexes but also whether the field-stop layers are influenced by annealing at elevated temperatures.

2 Physical basics

Whenever the periodicity in a perfect single crystalline structure is perturbed, discrete energy levels E_T are introduced which may be located within the forbidden band-gap. This is shown in Fig. 2.1. In general, lattice defects are classified according to their spatial expansion. One distinguishes between point, line, planar and bulk defects. Point defects may be extrinsic like foreign interstitial or substitutional atoms but also intrinsic like self-interstitials or vacancies. A further differentiation is made between shallow levels and so called deep-levels: The introduction of doping atoms, like B or P in Si, which is very common to increase the conductivity, causes shallow levels very close to the valence or conduction band, respectively. Deep-levels in contrast lie, as the name suggests, much deeper within the band-gap where they can act as generation-recombination (G-R) centers or so-called carrier traps.

The occupancy of a deep trap with energy E_T can be changed via four different interactions with the valence (E_V) or conduction band E_C. They are depicted in Fig. 2.1. After an electron gets captured from the conduction band, as shown in Fig. 2.1 (a) it may either be re-emitted to the conduction band (Fig. 2.1 (b)) or a hole can be captured from the valence band (Fig. 2.1 (c)). In both cases the trap is occupied by a hole afterwards which again can either be emitted back to the valence band, as in Fig. 2.1 (d), or an electron can be captured from the conduction band (Fig. 2.1 (a)). Process (a) followed by process (c) is called recombination while process (b) followed by process (d) is called generation. Therefore in G-R events the deep-level trap and *both*, the valence and the conduction band are participating. In contrast to this in trapping events either valence *or* conduction band are interacting. To summarize these are process (a) followed by (b), or (c) followed by (d) and they are neither recombination nor generation [29].

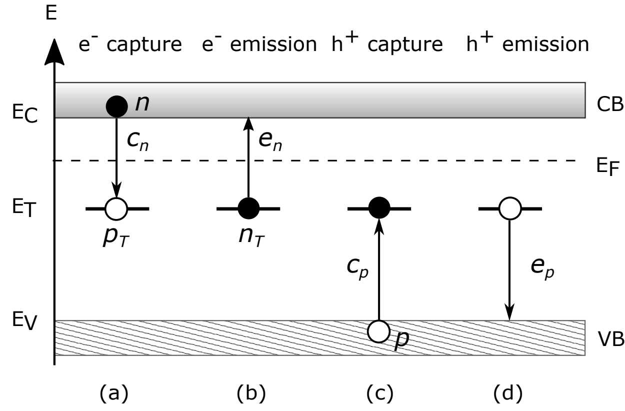

Figure 2.1: The four possible transitions between the semiconductor band edges and the deep impurity level E_T: (a) electron capture, (b) electron emission, (c) hole capture, (d) hole emission.

According to the Shockley-Read-Hall (SRH) model these transitions are statistical processes depending solely on the concentration of participating charge carriers [34]. The change of electron density in the conduction band n with time is given as the difference between electron capture and emission

$$\frac{dn}{dt} = (b) - (a) = e_\text{n} n_\text{T} - c_\text{n} n p_\text{T} \tag{2.1}$$

where e_n and c_n are the electron emission and capture rate, respectively, p_T is the density of traps occupied by holes and n_T is the density of traps occupied by electrons. While electron emission depends solely on e_n and n_T, the capture process is additionally limited by the number of electrons in the conduction band n.

Furthermore, the expression for the density of holes in the valence band is given by

$$\frac{dp}{dt} = (d) - (c) = e_\text{p} p_\text{T} - c_\text{p} p n_\text{T} \tag{2.2}$$

with e_p and c_p, the hole emission and capture rate.

The capture coefficients are defined as

$$c_\text{n} = \sigma_\text{n} v_\text{th,n} \qquad\qquad c_\text{p} = \sigma_\text{p} v_\text{th,p}$$

with the thermal velocity v_th and the capture cross section σ of the trap for electrons (n) and holes (p).

Considering all four possible transitions between trap states and semiconductor band edges, the change of trap occupancy with time is given by

$$\frac{dn_T}{dt} = \frac{dp}{dt} - \frac{dn}{dt} = (c_n n + e_p)(N_T - n_T) - (c_p p + e_n) n_T \tag{2.3}$$

where N_T is the total number of defect states and n_T is the density of trap levels occupied by electrons. The solution of this differential equation yields

$$n_T(t) = n_T(0) \exp\left(\frac{-t}{\tau}\right) + \frac{(c_n n + e_p) N_T}{c_n n + e_p + c_p p + e_n} \left[1 - \exp\left(\frac{-t}{\tau}\right)\right] \tag{2.4}$$

where $n_T(0)$ is the initial density of occupied traps and τ is defined as

$$\tau = \frac{1}{c_n n + e\text{p} + c_p p + e_n}. \tag{2.5}$$

In this thesis all measurements were performed measuring (mainly electron-) emission processes within the space-charge region in p^+/n diodes. Since the depletion region in such structures extends mainly to the n-side of the diode, further simplifications can be made. Neglecting p-type volume activity and considering only traps in the upper half of the band gap, which applies for $e_n >> e_p$, Eq. 2.4 reduces to

$$n_T(t) \approx N_T \exp\left(-\frac{t}{\tau_e}\right) \tag{2.6}$$

with $\tau_e = 1/e_n$ assuming fully filled trap occupation.

3 Platinum deep levels in silicon

Two deep levels caused by platinum occupying substitutional sites in the silicon lattice were assigned: an acceptor level 0.23 eV below the conduction band as well as a donor level 0.36 eV above the valence band [15, 20, 27, 28]. According to literature [15, 20] Pt diffusion into Si occurs mainly via the so-called kick-out mechanism. Pt interstitial atoms Pt_i are able to move very fast within the host lattice so that they can gain enough kinetic energy to eventually kick-out one atom of the host-lattice. The kicked-out Si then takes a place as self-interstitial Si_I while the former interstitial Pt occupies the substitutional site Pt_s:

$$Pt_i \longleftrightarrow Pt_s + Si_I. \qquad (3.1)$$

Since the surface acts as an efficient sink of silicon self-interstitials, the formation of substitutional Pt happens preferentially in the vicinity of the surface resulting in a symmetric U-shaped concentration profile even if the Pt is applied only at one side of the sample. A typical depth profile of Pt-diffused Si is depicted in Fig. 3.1. As predicted by the kick-out mechanism [6] the substitutional Pt concentration in the middle of the sample increases with the square root of the annealing time t.

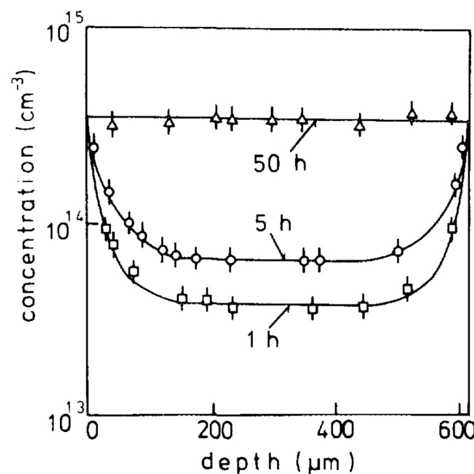

Figure 3.1: Concentration profiles of the E_C−0.23 eV level in Pt-diffused Si at 900 °C for different diffusion times [15].

4 Experimental techniques

4.1 Deep-Level Transient Spectroscopy (DLTS)

Deep-level transient spectroscopy is a powerful and sensitive method to investigate trap levels in semiconductors which are located deep within the forbidden band-gap. The technique was developed by D.V. Lang [16] in 1974 and is based on changing the occupancy of trap states in the space-charge region by varying the applied voltage. Therefore a device is needed which is capable of building up a depletion region such as Schottky- or pn-diodes. In this thesis all measurements are performed on p^+/n Si diodes. The pn-junction capacitance can be described by the equation of a parallel plate capacitor with the depletion region acting as dielectric:

$$C = \frac{\epsilon_{\mathrm{Si}} A}{W} \tag{4.1}$$

where ϵ_{Si} is the permittivity of silicon, A is the diode area and W is the depletion width.

Deep traps in the semiconductor have an influence on the width of the space-charge region, therefore changing their occupancy causes a capacitance transient which is monitored as a function of time at a fixed temperature. This procedure is repeated for a number of different temperatures. Further data analysis yields a spectrum of all the trap states in the crystal as a function of temperature. From the sign of the peaks one is able to distinguish between majority- and minority carrier traps, their peak height is proportional to the trap concentration. Information like the electron- and hole capture cross-section or the trap level position in the band-gap with respect to valence or conduction band can also be obtained.

4.1.1 Measurement principle

The DLTS measurement is based on changing the occupancy of deep traps in the depletion region of a pn- or Schottky-diode by switching the applied bias between a filling pulse voltage V_{f} and a recovery pulse voltage V_{r}. The recovery pulse is always a large reverse bias whereas the filling pulse can be anything between a small forward bias (MCTS) and a reverse bias smaller

than the recovery pulse (conventional DLTS). The principle is explained in Fig. 4.1 using a p^+/n junction with electron traps in the space-charge region.

4.1.2 Steady-state reverse bias

Fig. 4.1 a) shows the steady state condition for a pn diode biased with a high reverse voltage V_r. In the depletion region, $n \approx p \approx 0$ since carriers are swept out by the electric field. Furthermore the trap level E_T is above the Fermi-level $E_{F,n}$ in the region $0 < x < W_R - \lambda$ which is why the traps within this area are not occupied by electrons in steady state reverse bias. Nevertheless, as one approaches the neutral semiconductor there is a region within depletion zone where $E_T < E_{F,n}$. Within $W_R - \lambda < x < W_R$ the traps remain filled also during the emission phase. This transition region is taken into account in further analysis and is referred to as 'lambda-correction'. Neglecting it would lead to an underestimation of the actual trap concentration within the depletion region.

4.1.3 Filling of the traps

When the reverse bias is reduced by applying a filling pulse V_f of 0 V (see Fig. 4.1 b)) the bands straighten out and traps within $W_p - \lambda < x < W_R - \lambda$ get filled with electrons following the exponential capture law described in Eq. 2.4. Traps within $0 < x < W_p - \lambda$ are never filled using 0 V as filling pulse since $E_T > E_{F,n}$. According to [18] the required pulse width to fill all traps depends on the capture cross section σ_n of the trap level. The larger σ_n is, the shorter is the required pulse. In this thesis filling pulses larger than 1 ms were found to be sufficient to reach the saturation of trap occupation as discussed later.

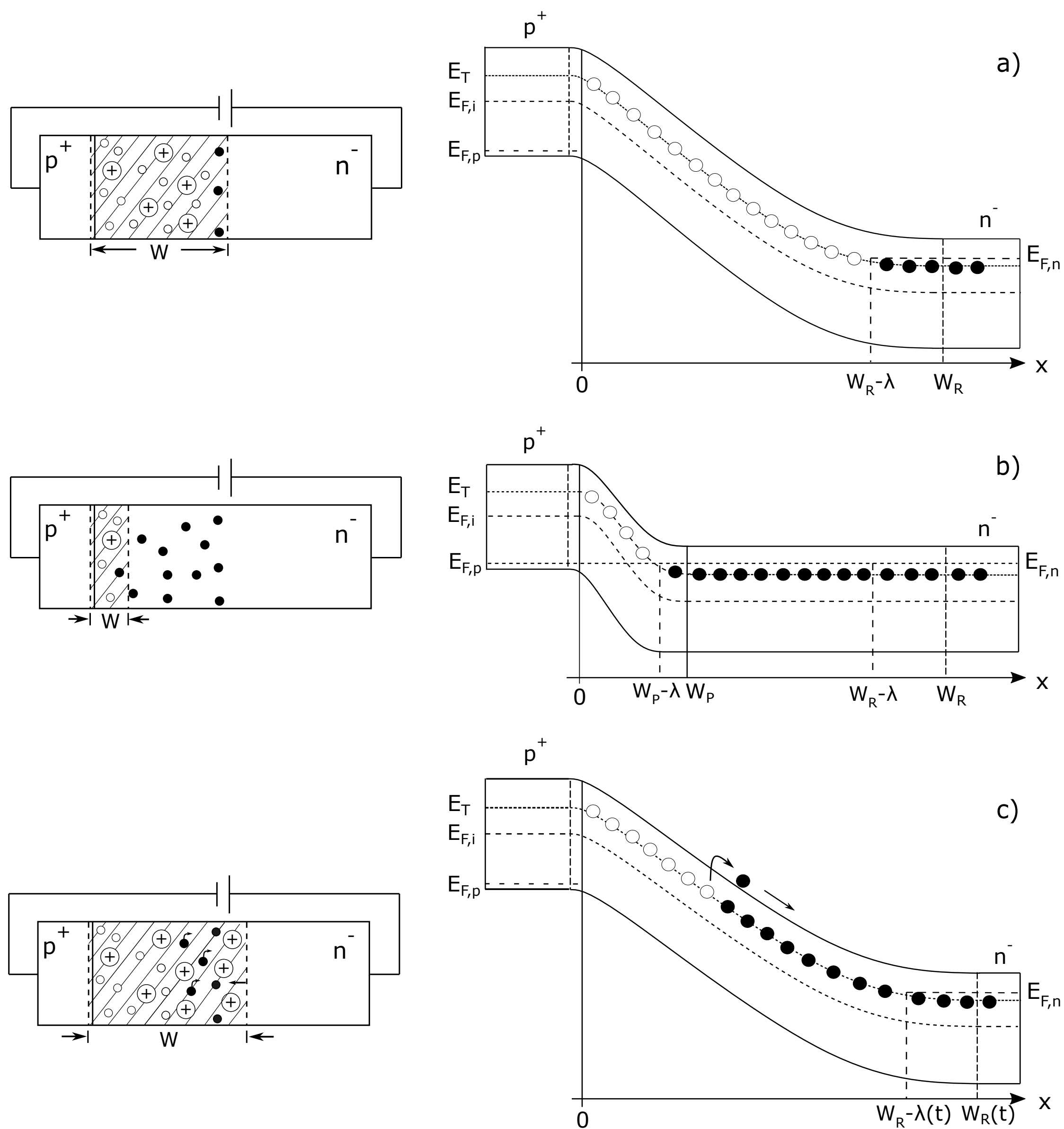

Figure 4.1: DLTS measurement principle explained on a p^+/n diode and corresponding band diagram: a) steady-state reverse bias, b) filling pulse $V_f = 0$ V, c) electron emission from traps shortly after switching back to high reverse bias V_r.

4.1.4 Electron emission

Initially, after switching the applied bias from V_f to V_r all the traps are filled with electrons and the depletion region is larger, than it was in steady state reverse bias to compensate the

additional trapped charge. But since E_T is now above $E_{F,n}$ again, the traps start to emit the captured electrons. This is a thermally activated process described by [1]

$$e_n = \sigma_n v_{th} N_C \exp\left(-\frac{E_C - E_T}{kT}\right). \tag{4.2}$$

Now formerly trapped electrons immediately drift to the n-type material causing the space-charge region to shrink again. As depletion width and capacitance are inversely proportional according to Eq. 4.1 the decrease of depletion width can be measured as capacitance transient as depicted in Fig. 4.2.

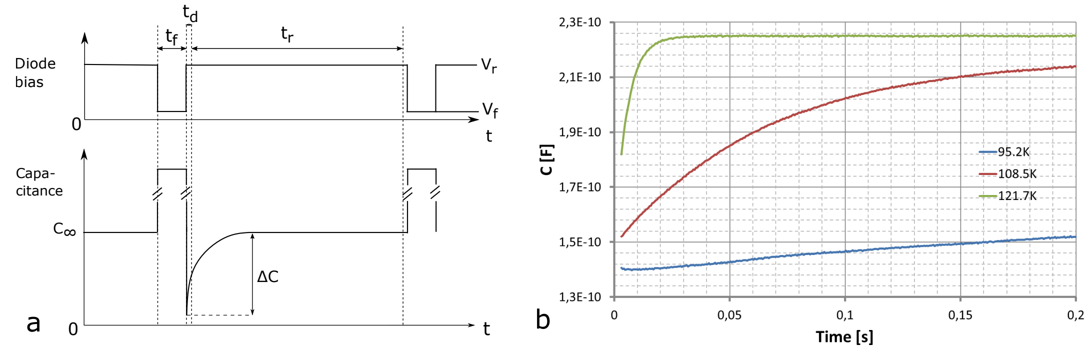

Figure 4.2: Capacitance response to switching of bias voltage for a p$^+$/n diode

The whole procedure is repeated several times during a temperature scan and the capacitance transient is measured at each temperature. In this thesis a temperature range from 20 - 300 K is used.

4.1.5 Capacitance transients

Considering an abrupt, one-sided p$^+$/n junction and assuming uniform doping concentration the capacitance can be described as

$$C = \epsilon A \left[\frac{qN}{2\epsilon(V_{bi} - V)}\right]^{\frac{1}{2}} = \epsilon A \left[\frac{q(N_D - n_T)}{2\epsilon(V_{bi} - V)}\right]^{\frac{1}{2}} \tag{4.3}$$

.

This expression can be rearranged to

$$C = C_\infty \left(1 - \frac{n_T}{N_D}\right)^{\frac{1}{2}} \tag{4.4}$$

.

If $N_T \ll N_D$ is valid, this equation can be further simplified yielding

$$C(t) = C_\infty \left(1 - \frac{n_T(t)}{2N_D}\right) = C_\infty \left[1 - \frac{N_T}{2N_D} \exp\left(\frac{-t}{\tau_e}\right)\right] \tag{4.5}$$

.

In the last expression Eq. 2.6 was inserted for $n_T(t)$.

In general one assumes all traps to be filled at $t = 0$ (after switching from V_f to V_r), therefore $n_T(0) = N_T$ and $e_p = 0$ which means that all traps are empty at $t = \infty$ such that $n_T(\infty) = 0$. Rearranging Eq. 4.5 and using the mentioned relations following equation can be derived

$$N_T = \frac{2N_D \Delta C}{C_\infty} \tag{4.6}$$

where ΔC is defined as $C(\infty) - C(0)$. Eq. 4.2 can be rearranged to

$$\ln(\tau_e T^2) = (E_C - E_T)\frac{1}{kT} - \ln\left(N_C^* v_{th}^* \sigma_n\right). \tag{4.7}$$

In the above equation $v_{th}^* = \frac{v_{th}}{T^{1/2}}$ and $N_C^* = \frac{N_C}{T^{3/2}}$ to get rid of the temperature dependency of the thermal electron velocity and the effective density of states in the conduction band. This is necessary to obtain the form of a linear equation. Once one has extracted a set of τ_e and the corresponding temperatures T of a certain peak maximum from the measurement data, the energy level E_T of the trap with respect to the conduction band as well as the capture cross section σ_n can be obtained from an Arrhenius plot.

4.1.6 DLTS analysis

The DLTS signal $S(T)$ is obtained by monitoring the capacitance transients at different temperatures within a certain time window and forming the difference at, for instance using a boxcar integration, t_1 and t_2

$$S(T) = C(t_1) - C(t_2) = \Delta C \left(\exp\left(-\frac{-t_1}{\tau_n}\right) - \exp\left(-\frac{-t_2}{\tau_n}\right)\right). \tag{4.8}$$

Typical capacitance transients and the resulting DLTS spectrum which is $S(T)$ applied over T are depicted in Fig. 4.3. The lower limit for the start time of observation t_1 is given by the measurement instrument. Due to this delay time t_d (also visible in Fig. 4.2) it is not possible to monitor the transient from the very beginning.

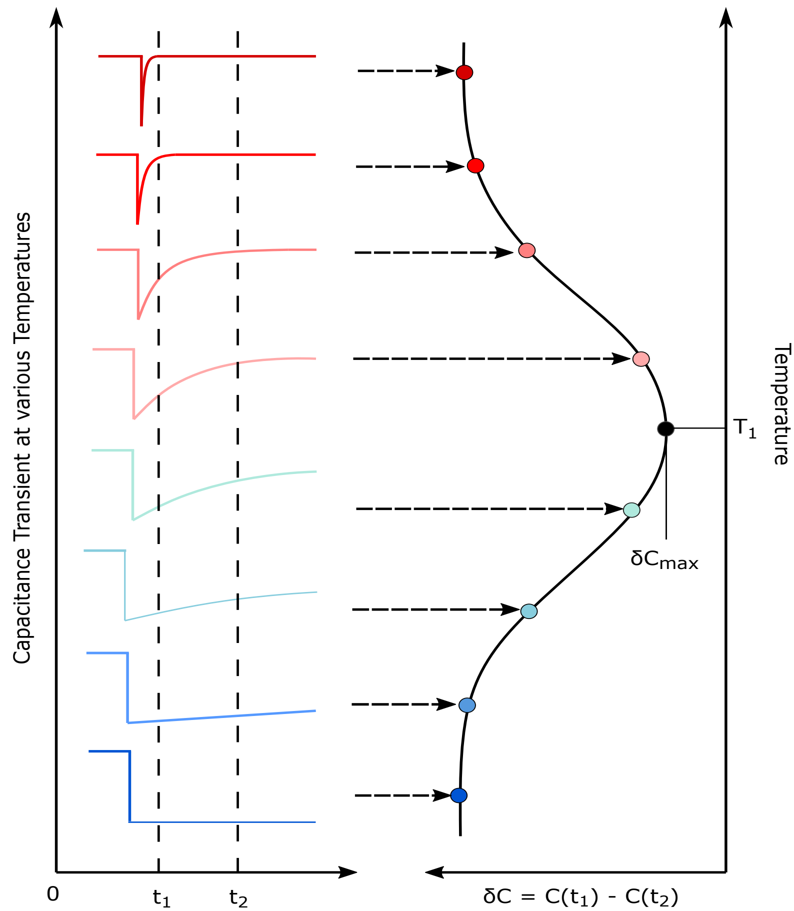

Figure 4.3: Left: typical capacitance transients at different temperatures, right: DLTS spectrum obtained from transients

Since the emission process is thermally activated, the emission rate constant τ_e of the traps can be varied by changing the temperature. The capacitance returns to steady state capacitance C_∞ very fast at elevated temperatures. That is why the transient can lie completely out of the observation time window at high temperatures yielding a δC of zero. For lower temperatures the emission time constant τ_e of the traps is larger resulting in a higher change in capacitance can be recorded. At very low temperatures, in contrast, the transient is so slow that the capacitance is again approximately constant during the measurement time window, see Fig. 4.3.

If the time constant set by the measurement time window is in the order of τ_e of the trap, the DLTS signal $S(T)$ yields a maximum. The value of this time constant at maximum DLTS signal can be derived by forming the derivative of Eq. 4.8 with respect to τ_e and setting the result to zero

$$\tau_{\text{n, max}} = \frac{t_1 - t_2}{\ln(t_2/t_1)}. \tag{4.9}$$

The expression $e_{\text{n, max}} = \tau_{\text{n, max}}^{-1}$ is in general referred to as rate window [16]. The temperature position of the maximum in the DLTS spectrum depends on the type of the defect and on the rate window. This means that by varying t_1 and t_2 one can shift the position of the DLTS peak within a certain range.

$\tau_{\text{n, max}}$ and the corresponding temperature can be used as a first point in an Arrhenius plot. According to Eq. 4.7 the trap level E_T as well as the capture cross section σ_{th} can be extracted by plotting the logarithm of $\tau_e T^2$ against $1/k_B T$. Therefore several measurements with different rate windows, i.e. different times t_1 and t_2 are necessary. Another method for obtaining several time constants τ_e is the use of correlation or weighting functions on one set of capacitance transients.

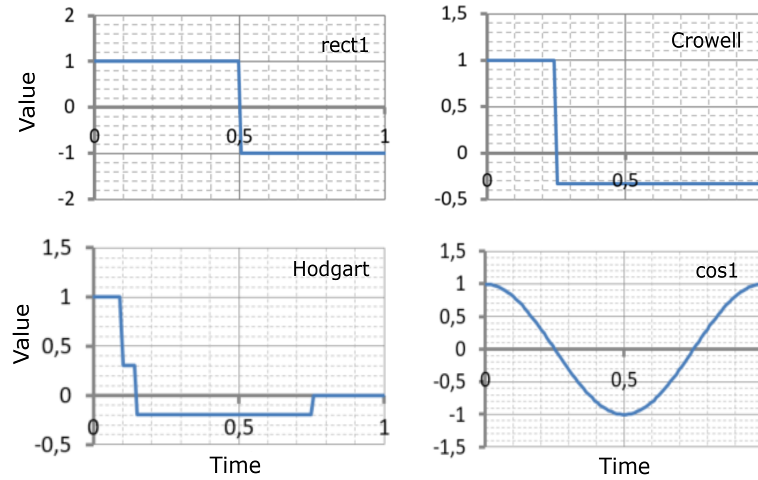

Figure 4.4: Some of the correlation functions used for DLTS signal analysis.

This is also a widespread approach to improve the signal to noise ratio. The DLTS spectrum is obtained by multiplying the capacitance transients with certain weighting functions $w(t)$ and integrating the product

$$S(T) = \int w(t) C(t, T) dt. \tag{4.10}$$

Possible correlation functions are rectangular, sine or cosine functions (see Fig. 4.4). Each weighting function has its characteristic time constant τ_e leading to a DLTS peak at different T and therefore to further points in the Arrhenius plot as depicted in Fig. 4.5.

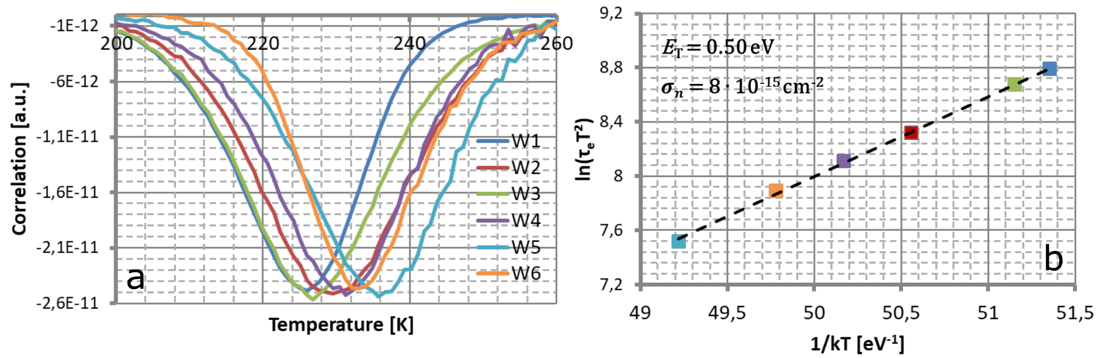

Figure 4.5: Illustration of the influence of different correlation functions on the DLTS spectrum (left). Plotting $\ln(\tau_e T^2)$ vs the corresponding temperature T for each correlation function yields the Arrhenius plot (right).

Applying a linear fit on the data of the Arrhenius plot in Fig. 4.5 allows to extract certain trap properties. Considering Eq. 4.7 the slope of the fitting function yields the position of the trap level within the band gap, often also referred to as activation energy of the trap E_A, whereas the intercept of the linear fit with the y-axis contains the capture-cross section σ_n.

4.1.7 Influence of measurement parameters on the DLTS spectrum

- **Recovery time** t_r**:** The recovery time means the difference $t_2 - t_1$ (see Fig.4.3). The measurement system used keeps a fixed ratio t_1/t_2 of 0.01, therefore by varying t_r one changes t_1 as well as t_2. Fig. 4.9 b) and Fig. 4.2 b) clearly show the influence of temperature on the transients. Lower temperatures slow down the emission of electrons from the trap states and thus the capacitance response. They therefore allow to detect emission processes that happen too fast at room temperature and above by decreasing the emission rate. Understanding this relation is necessary to explain the influence of the recovery time t_r on the DLTS spectrum: Increasing t_r causes a larger measurement time window but at the same time also increases t_1, which leads to delayed recording of the capacitance (or current) transient. Since emission processes happen faster at higher T the main part of the transient may lie already out of the measurement time window for larger t_1. Consequently, an increase of the recovery time t_r shifts peaks in the DLTS

spectrum towards lower temperatures while peak height and form remain unchanged. This is depicted in Fig. 4.6 and can be explained by considering Eq. 4.9.

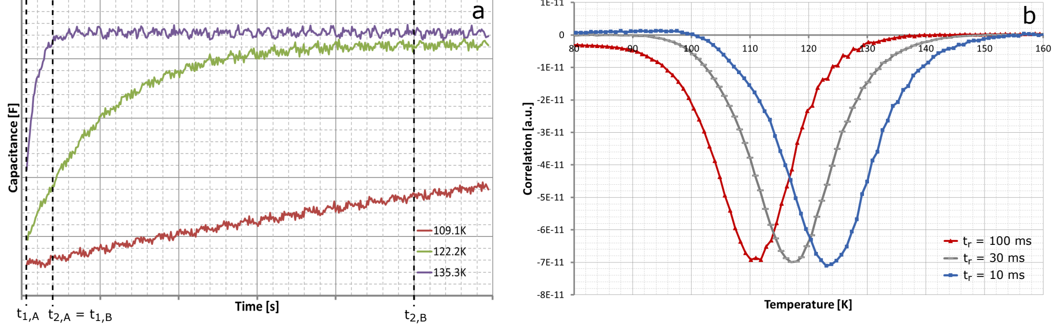

Figure 4.6: Influence of increasing t_r: The start of transient recording t_1 is delayed leading to a cut off of the main part at high temperatures - ΔC within measurement time window is larger at low T (a). DLTS peak is shifted towards lower T (b).

- **Filling pulse duration t_f:** As already mentioned above, the filling pulse has to be applied for a sufficiently long time to ensure that all the traps are filled with electrons. If a too short t_f is chosen, trap states remain empty which leads to an underestimation of the actual defect concentration. For point defects, in theory an exponential filling behaviour according to [1]

$$n_T(t) = N_T(1 - \exp(-c_n n t)) \tag{4.11}$$

is expected. In this equation t counts from the beginning of the filling pulse. Therefore $n_T = N_T$ if $t \to \infty$. Eq. 4.11 corresponds to a capacitance change ΔC of

$$\Delta C(t) = \Delta C_{max}\left(1 - \exp\left(\frac{-t}{\tau_c}\right)\right) \tag{4.12}$$

where ΔC_{max} is the maximum change of capacitance due to complete filling of traps. Investigation of capture kinetics is done by observing the DLTS peak height as a function of filling pulse duration. The measured behaviour is depicted in Fig. 4.7. The concentration of filled traps shows a logarithmic dependence on filling time until saturation starts at sufficiently long pulses. It is observed that saturation is obtained for filling times longer than 1 ms. For a correct trap concentration determination saturation of filled defect levels is crucial. Too short t_f otherwise lead to underestimation of the actual number of traps.

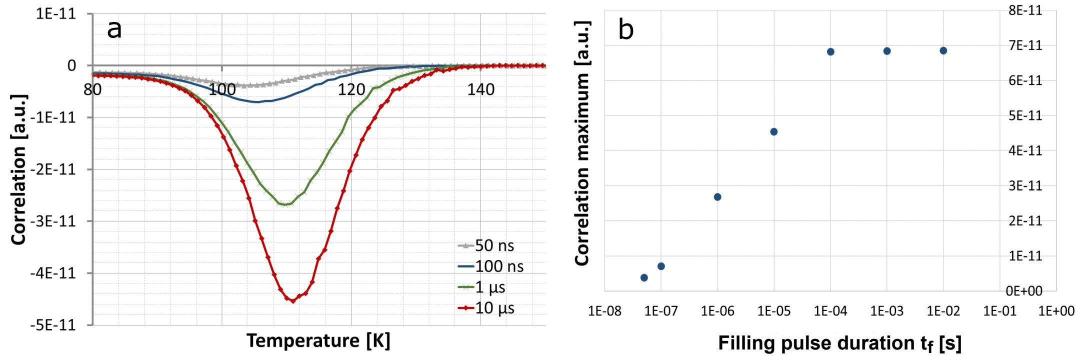

Figure 4.7: Influence of filling pulse duration t_f on the DLTS spectrum: Longer filling pulses cause an increase of the DLTS peak maximum corresponding to a higher number of traps filled with electrons (a). The number of filled traps increases logarithmically with t_f until after sufficiently long filling pulses all the traps are filled with electrons and saturation is reached (b).

The same behaviour has already been measured by Pons [26] and Lauwert et al. [17]. They explain the non-exponential capture kinetics by the refilling in the potential barrier remaining during filling pulse [26], also referred to as capture in the "Debye-tail" which means the transition zone between neutral semiconductor and depletion region. Also, according to Zylberszteijn [36] the kinetics can be described as a "fast" purely exponential part due to capture within the neutral semiconductor with homogeneous capture rate $c_n n$ and a "slow" part. The slow part corresponds to capture within Debye tail where a distribution of capture rates $c_n n(x)$ exists since the density of free carriers varies strongly with position x from N_D close to depletion edge, to zero a few Debye lengths within the space-charge region. Usually, attempts are made to minimize the contribution of the slow part by choosing a small forward bias as filling pulse and a high reverse voltage as recovery pulse. Nevertheless, capture in the Debye tail accounts for at least ten percent of the total capture kinetics [26].

- **Recovery pulse voltage V_r:** The space-charge region width of a p^+/n-junction can be found from depletion approximation [32]:

$$W = \sqrt{\frac{2\epsilon_{Si}(V + V_{bi})}{qN_D}}. \tag{4.13}$$

The recovery pulse voltage thus sets the penetration depth of the space-charge region and therefore the measured volume. This allows for the determination of trap density depth profiles as explained in more detail in 4.1.11.

- **Filling pulse voltage V_f:** Similar to V_r also the filling pulse voltage V_f can be used to enlarge or narrow the measurement volume. Furthermore, the sign of the V_f defines the type of investigated traps. A mere reduction of applied bias from V_r to a lower reverse voltage V_f will allow only majority carrier traps to be filled and detected. However, by applying forward bias also minority carrier traps can be detected. This measurement method is called minority carrier transient spectroscopy (MCTS).

4.1.8 Minority Carrier Transient Spectroscopy (MCTS)

The conventional DLTS methodology described above is only capable of detecting traps in the upper (lower) half of the band-gap in n-type (p-type) semiconductors on Schottky contacts. Considering the p^+/n diode again, applying a small forward bias injects holes into the n-region and fills the minority carrier traps which also emit their holes again as the applied bias is switched to a large reverse bias. Minority carrier traps cause a positive peak in the MCTS spectrum, whereas majority carrier traps cause a negative peak. A typical MCTS spectrum is shown in Fig. 4.8.

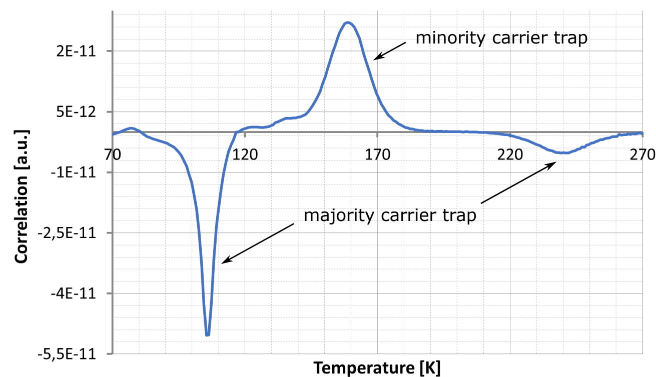

Figure 4.8: MCTS spectrum of a p^+/n diode. Minority carrier (hole) traps show up as positive peaks while majority carrier (electron) traps cause a negative peak in the spectrum.

4.1.9 Current Transient Spectroscopy (IDLTS)

A further technique is the current transient spectroscopy (IDLTS). The basic principle is the same as for the standard (capacitance) DLTS but instead of measuring the emitted charge carriers as capacitance transient they are measured as current. When the applied reverse bias is reduced during the filling pulse a sharp, short current peak can be observed which are electrons flooding parts of the former depletion region and instantly recombining with the ionized dopant atoms respectively filling the traps. After switching back to V_r at first electrons

are swept out of the space-charge region due to the electric field very fast. Afterwards the traps start to emit the electrons with a little time delay. Despite of the time dependence the two current components can also be distinguished due to the temperature dependence of the electrons emitted by the traps. The exponential current transient is depicted in Fig. 4.9 and according to [3] given by

$$I(t) = \frac{q\Delta W A N_{\mathrm{T}}}{2\tau_{\mathrm{e}}} \exp^{-\frac{t}{\tau_{\mathrm{e}}}} + I_{\mathrm{L}} \tag{4.14}$$

where I_{L} is the steady-state diode leakage current at V_{r} and ΔW is the width of the measurement volume, $W(V_{\mathrm{r}}) - W(V_{\mathrm{f}})$. The current therefore is directly proportional to the trap concentration within the observed region. In Fig. 4.9 it can be clearly seen how low temperatures slow down the carrier emission process.

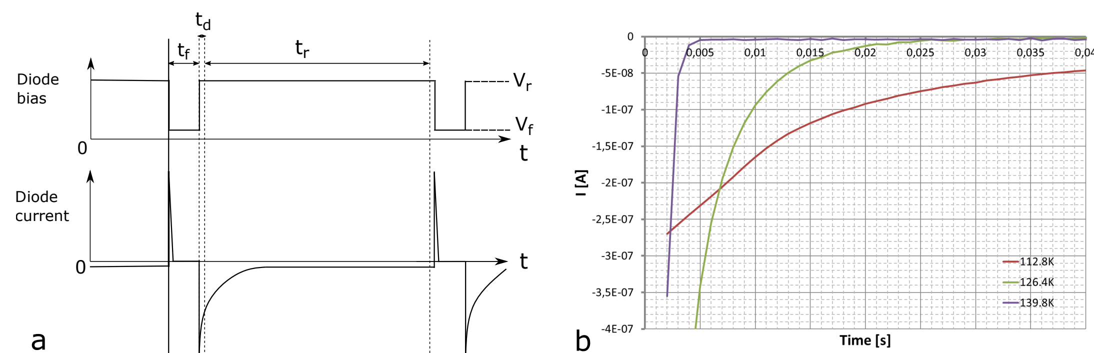

Figure 4.9: Majority carrier filling pulse and current response for a p^+/n diode (a). Actually measured data - current transients at different measurement temperatures (b).

The disadvantage of IDLTS is that minority and majority carrier traps cannot be distinguished.

4.1.10 Constant-capacitance DLTS (CCDLTS)

In contrast to the conventional DLTS measurement, the capacitance and therefore the depletion width is held constant during the carrier emission process in CCDLTS. This is done by using a feedback loop which dynamically varies the applied voltage such that the capacitance stays constant. The trap information in CCDLTS is extracted from the time-varying voltage curves. One assumption in the analysis of conventional DLTS data is that $N_{\mathrm{T}} \ll N_{\mathrm{D}}$. For $N_{\mathrm{T}} > 0.1 N_{\mathrm{D}}$ Eq. 4.5 loses its validity since large changes in W cause the C-t signal to become non-exponential [29]. From Eq. 4.3 one obtains the relation between voltage and trap concentration N_{T}

$$V = -\frac{q\epsilon A}{2C^2}\left(N_\mathrm{D} - N_\mathrm{T}\exp\left(-\frac{t}{\tau_\mathrm{e}}\right)\right) + V_{bi} \tag{4.15}$$

which is not subject to this limitation. This equation holds true for arbitrary high N_T because the depletion width is held constant and instead of the capacitance the voltage change is a direct measure of the trap concentration.

4.1.11 Depth profiling with DLTS

As it is visible in Fig. 4.1 only traps within $W_\mathrm{R} - \lambda$ and $W_\mathrm{P} - \lambda$ change their occupancy on varying the applied voltage. This can be utilized to accurately set the range to be investigated. In principle one has three possibilities to do so: change the filling pulse V_f and keep the recovery pulse V_r fixed, vary V_r and keep V_f constant or change V_f as well as V_r. Both last-mentioned variants have the drawback that the traps near the depletion region border close to the neutral semiconductor show non-exponential emission behaviour which complicate the analysis. This phenomenon is often referred to as "Debye tailing" [26, 17] and can lead to misinterpretation of the actual trap concentration. In this thesis the first method was chosen for depth profiling. By forming the difference between signals of two different V_f only traps within a width of ΔW_R (see Fig. 4.10) are recorded. Furthermore it is made sure that only traps within the actual depleted region contribute to the signal and the influence of the Debye-tail is neglected. The calculated mean trap concentration is applied over the mean distance from pn-junction $\bar{x}$ to obtain the depth profile.

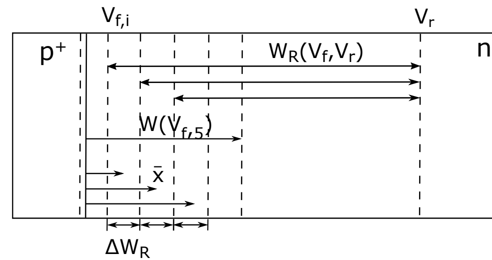

Figure 4.10: Schematic representation of depth profiling on a p$^+$/n junction with DLTS. V_f is varied to investigate different sections of the depletion region. V_r is held constant.

4.2 Capacitance-voltage (CV) measurements

The pn-junction capacitance can be expressed by the equation of a parallel plate capacitor with the depletion width W as distance between the plates and the semiconducting material as dielectric

$$C = \frac{\epsilon_{\text{Si}} A}{W} = A \left[\frac{q\epsilon_{\text{Si}}}{2(V_{\text{bi}} - V)} \frac{N_{\text{A}} N_{\text{D}}}{N_{\text{A}} + N_{\text{D}}} \right]^{\frac{1}{2}}. \tag{4.16}$$

This can be rearranged to obtain a linear dependence from applied voltage yielding

$$\frac{1}{C^2} = \frac{2}{q\epsilon_{\text{Si}}} \frac{N_{\text{A}} + N_{\text{D}}}{N_{\text{A}} N_{\text{D}}} (V_{\text{bi}} - V). \tag{4.17}$$

This expression allows to extract important parameters like the built-in voltage V_{bi} and the doping concentration N_{D} from a plot of $1/C^2$ vs V as depicted in Fig. 4.11 b). For a p^+/n junction ($N_{\text{A}} \gg N_{\text{D}}$), the donor concentration N_{D} is obtained from the slope of the curve as expressed by

$$N_{\text{D}} = -\frac{2}{q\epsilon_{\text{Si}}} \frac{1}{\frac{d(1/C^2)}{dV}} \tag{4.18}$$

while V_{bi} is given by the intersection of the $1/C^2$ curve with the x-axis.

In this thesis CV measurements were used to calculate the depletion width, to qualitatively estimate differences of similar diodes regarding their doping concentration and to gain information about the dopant depth profile. Experimental data showing a $1/C^2$ plot and the corresponding doping concentration depth profile can be seen in Fig. 4.11.

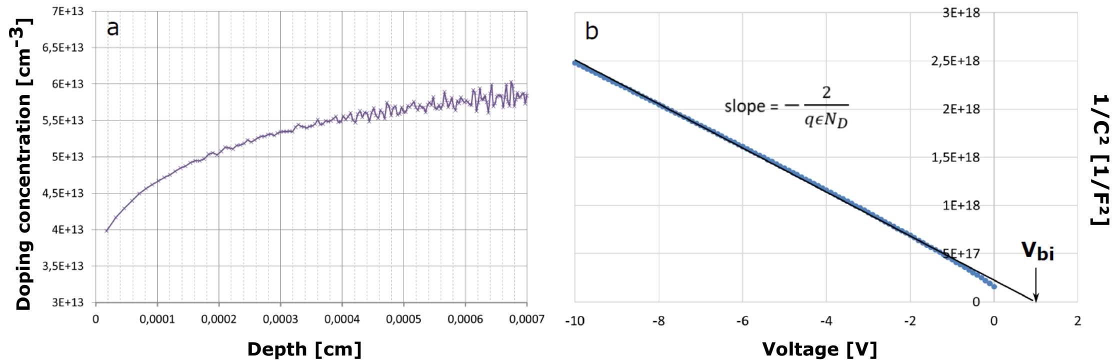

Figure 4.11: Donor concentration depth profile of a p^+/n diode calculated from the CV curve (a). $1/C^2$ plot for determination of V_{bi} and N_{D} (b).

4.3 Current-voltage (IV) measurements

Measuring the current-voltage characteristics in forward as well as in reverse bias was one of the methods used in this thesis for electrical characterization of the pn-diodes. For one-

dimensional pn-diodes the forward current as function of applied voltage can in good approximation be expressed by

$$I = I_{\text{diff}} \left(\exp \frac{qV}{\eta kT} - 1 \right) \tag{4.19}$$

where I_{diff} is the saturation value of the ideal diffusion current and η is the non-ideality factor which describes the deviation of a real diode from ideal-diode behaviour. Usually $1 < \eta \leqslant 2$.

In general, the reverse current I_R for applied bias not much higher than kT or at elevated temperature can be expressed as

$$I_R = I_{\text{diff}} + I_{\text{gen}} \tag{4.20}$$

with the generation current I_{gen}. For applied bias $V \gg kT$ the diffusion current can be neglected and the reverse current is mainly caused by generation which is why

$$I_R \approx I_{\text{gen}} = \frac{Aqn_i W}{\tau_g} \tag{4.21}$$

where τ_g is the generation lifetime. From this it is obvious that the reverse current increases linearly with the diode depletion width W and inversely proportional with τ_g [30].
Combining an IV-curve with a capacitance-voltage (CV) measurement of the same junction as proposed by [22] yields a graphical representation of Eq. 4.20. The reverse current density from the IV-measurement is applied over the depletion width calculated from the CV-measurement and 4.13 as depicted in Fig. 4.12 and is a simple method to separate the generation current I_{gen} from the saturation diffusion current I_{diff}.

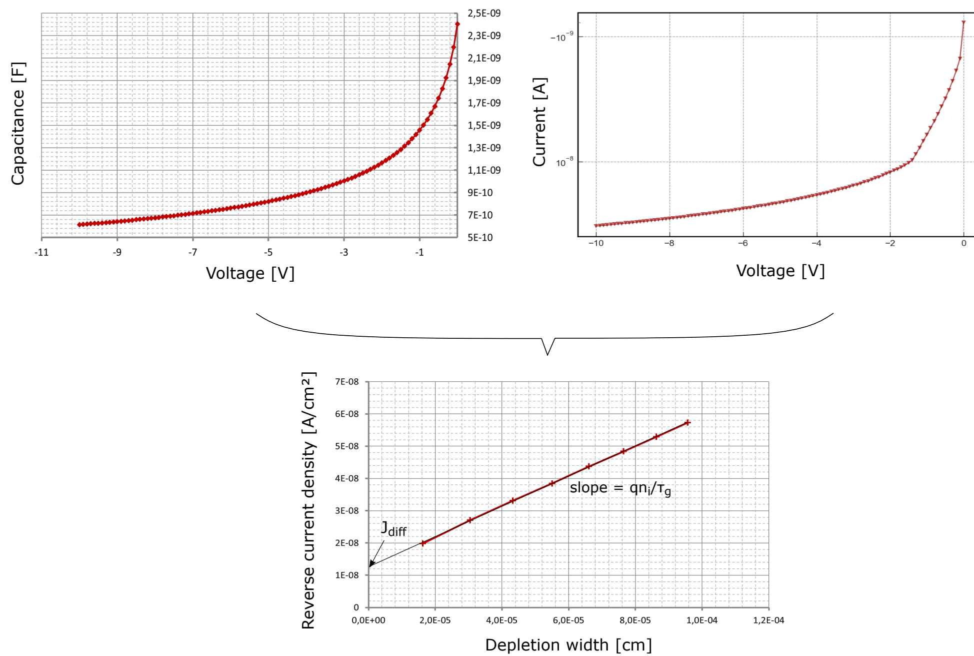

Figure 4.12: Graphical representation of the separation technique: IV and CV-curve (top) of the same junction in reverse bias are combined to separate the generation from diffusion current (bottom).

4.4 Spreading Resistance Profiling (SRP)

Nowadays the spreading resistance profiling technique is mainly used for the determination of resistivity and shallow dopant carrier concentration depth profiles. The measurement principle is depicted in Fig. 4.13. The device under test is beveled and two carefully aligned probes are stepped along the semiconductor surface. Typical bevel angles θ are 1°-5° for junction depths of 1-2 µm and $\theta \leq 0.5°$ for junction depths less than 0.5 µm [29]. For sample preparation the sample is fixed on a plunger using melted wax and then put into a metal cylinder above a rotating glass plate covered with a polishing compound. In this thesis the devices were lapped using a 0.10 µm diamond paste. Angle measurements are performed using an FPM precision goniometer.

The probes are aligned perpendicular to the bevel edge with a fixed distance to each other of about 32 µm. The resistivity is measured in equidistant steps of 5.0 µm. A weight of approximately 10 g is applied which is believed to be necessary to form good contact and break through the thin native oxide on the bevel surface [29]. Furthermore the probes form

imprints of about 10 nm depth which are necessary to count them and determine the starting point of the beveled surface. To reduce uncertainty of starting point determination a sharp bevel edge as well as an oxide coating of the original surface are helpful.

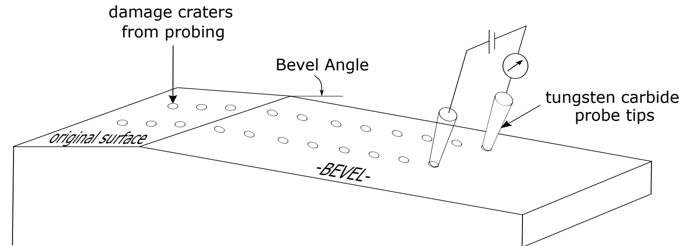

Figure 4.13: Beveled sample with probes and visible probing path

Due to the small probe tip to surface contact radius of about 5-10 µm the current spreads out radially in the sample as depicted in Fig. 4.14.

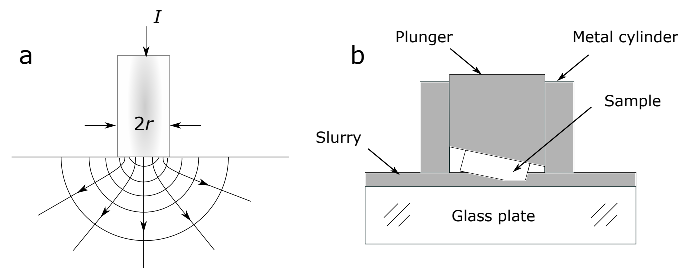

Figure 4.14: Cylindrical probe of diameter $2r$ in contact with a semiconductor, the arrows represent the direction of current flow (a). Bevel block for sample preparation (b).

The resulting resistance between the probes is given by

$$R = 2R_{\mathrm{p}} + 2R_{\mathrm{c}} + 2R_{\mathrm{sp}} \tag{4.22}$$

with the probe resistance R_{p}, the contact resistance R_{c} and the spreading resistance R_{sp}. For an indenting, pefectly conducting hemispherical probe tip with radius r in a homogeneous semi-infinite solid of resistivity ρ it could be shown [11, 21], that the spreading resistance R_{sp} is given by

$$R = \frac{\rho}{2\pi r s}. \tag{4.23}$$

In more general, the measured resistance R_{meas} can be described as

$$R_{\text{meas}} = R_{\text{c}} + \frac{\rho}{2r} C_{\text{srp}} \tag{4.24}$$

where C_{srp} is a correction factor taking into account the sample resistivity, probe radius, current distribution and probe spacing [29]. The obtained resistivity can then be related to the concentration of free charge carriers in the semiconductor:

$$\frac{1}{\rho} = \sigma = nq\mu_{\text{n}} + pq\mu_{\text{p}} \tag{4.25}$$

where σ is the conductivity and μ_{n} and μ_{p} are material specific electron and hole mobility, respectively. From that, for pure n-type material and in the case of fully ionized donors, the approximate doping concentration is given by

$$N_{\text{D}} \approx n \approx \frac{1}{\rho q \mu_{\text{n}}}. \tag{4.26}$$

4.5 Isothermal annealing

The annealing behaviour of a certain defect is in general a function of time and temperature. Investigating the concentration of defects as function of temperature and keeping the time constant is called isochronal annealing, while the variation of time at one fixed temperature is called isothermal annealing. A typical temperature curve for annealing measurements at two different temperatures as function of time (T-t curve) is depicted in Fig. 4.15. As one can see, the sample is not suddenly exposed to high temperature and after the annealing to room temperature again, but is has to undergo the heat up and cool down phase as well, which needs to be considered in the actual thermal budget. When performing the annealing experiment at different temperatures, the heat up and cool down is different for each temperature, while it is always the same for isothermal annealing measurement series. This is why only isothermal annealing was performed. The annealing time indicated refers to the time which the sample is held at the certain constant annealing temperature, thus does not include heat up and cool down phases. However, they are included in the fitting model.

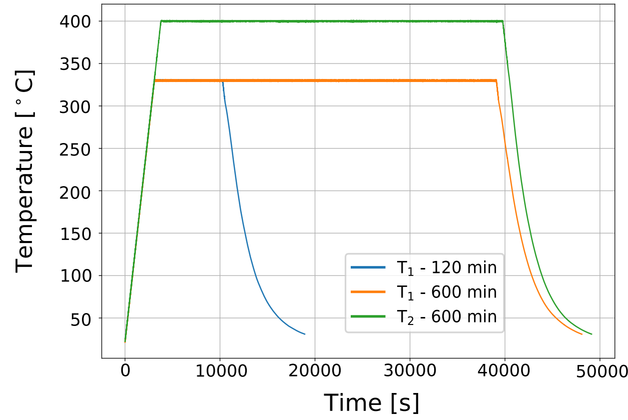

Figure 4.15: Temperature as a function of time during several annealing programs. Annealing at different temperatures adds different contributions to the thermal budget due to the differing development of T during heat up and cool down.

The dissociation of defect complexes with an initial concentration of $[A]_0$ at high temperatures can be described as first order reaction

$$\frac{\partial[A]}{\partial t} = -c(T)[A]^n \tag{4.27}$$

with order $n = 1$ and the reaction rate $c(T)$.

For first order decay, as which dissociation can be considered, the starting conditions are [18]:

$$[A](t=0) = [A]_{0,max} \tag{4.28}$$

$$[A](t=\infty) = [A]_{\infty,min}. \tag{4.29}$$

The solution is then given by

$$[A] = [A]_0 \exp(-c(T)t) = [A]_0 \exp\left(-c_0 \exp\left(-\frac{E_d}{kT}\right)t\right). \tag{4.30}$$

c_0 is the reaction rate constant which is independent of temperature and E_d is the reaction activation energy.

Measuring the defect concentration $[A]$ as a function of time for several isothermal measurement series yields the reaction rate $c(T)$ as slope of

$$\ln[A] = \ln[A]_0 - c(T)\,t. \tag{4.31}$$

Performing isothermal measurement series at different temperatures gives a set of reaction rates $c(T)$. By plotting $\ln c(T)$ in an Arrhenius plot as a function of $1/kT$ allows the determination of the activation energy E_a from the slope of

$$\ln c(T) = -\frac{E_\mathrm{d}}{kT} + \ln c_0 \tag{4.32}$$

while the intercept with the y-axis gives the reaction rate constant c_0.

5 Measurement instrumentation

5.1 Cryogenic probe station

The setup used for DLTS measurements consists of a Lakeshore CRX-6.5K probe station which is capable of measuring within a temperature range reaching from 20 K to 650 K, a Keithley 3390 pulse generator and a Zurich instruments HF2LI digital lock-in amplifier, which are operated by fully automatized Labview measurement software including a general user interface. The cryogenic probe station with all its major components is depicted in Fig. 5.1. It provides the temperature environment needed for the DLTS measurements as well as an electrical and optical interface with the sample.

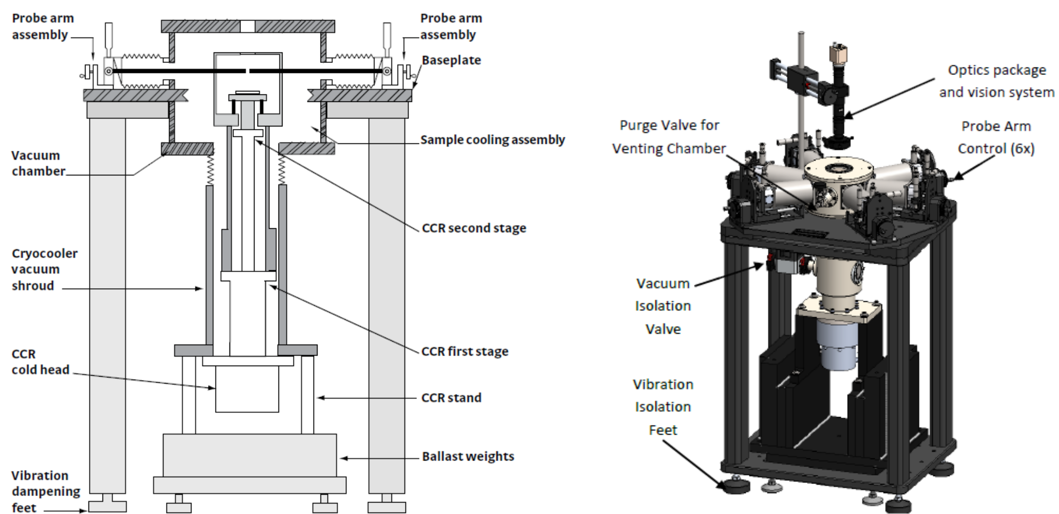

Figure 5.1: CRX-6.5K cryogenic probe station overview

The probe station contains a two-stage cooling assembly (outer shield and a radiation shield) using a closed cycle refrigerator (CCR) consisting of a helium compressor and a cold head. The vacuum chamber provides thermal insulation for the cryogenic cooling system (vacuum at base temperature 10^{-5} mbar). There are four electrical probe connections as well as a chuck connection via triax cable available. The probes are needles made of tungsten with a tip radius

of 25 µm. A microscope, a colour CCD camera and a monitor build the optical interface with the sample.

Fig. 5.2 shows the full DLTS measurement setup including a helium compressor, a vacuum pump, a temperature controller, a lock-in amplifier, a pulse generator and the cryogenic probe station already described in 5.1. Constant heating or temperature ramping is performed by the temperature controller using calibrated temperature sensors embedded in the chuck.

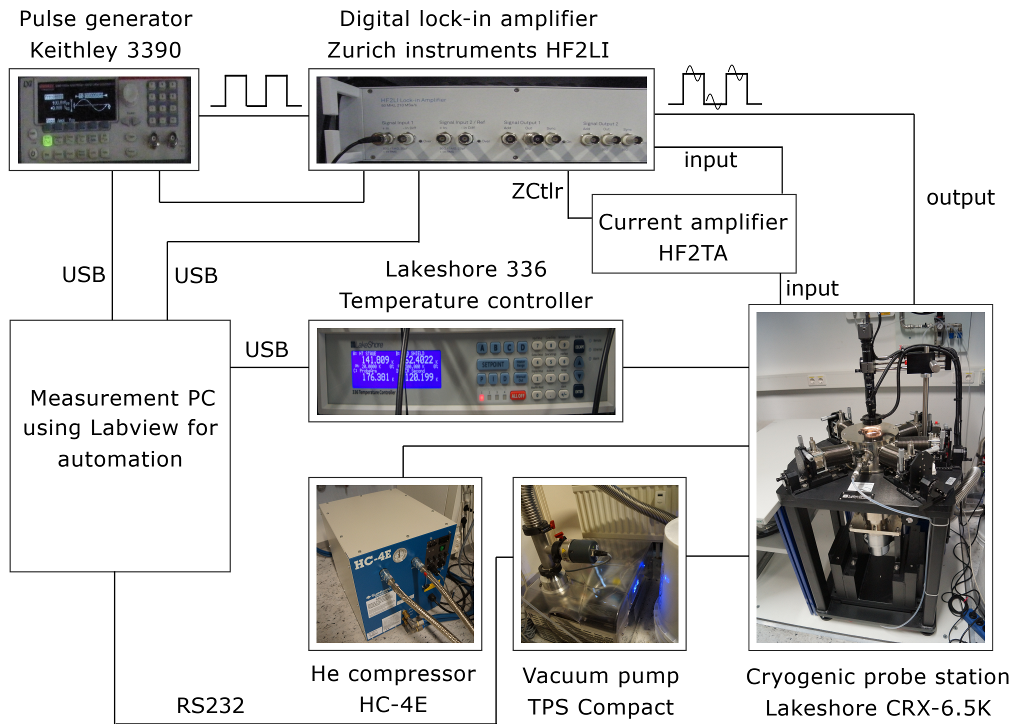

Figure 5.2: Full DLTS measurement setup.

5.2 Waferbow measurement station

Isothermal annealing experiments were performed using a furnace normally constructed and used for measurements of wafer curvature e.g. of copper coated silicon wafers exposed to high temperatures. The setup is depicted in Fig. 5.3. There have to be at least two samples put into the measurement chamber - one is used solely for temperature measurements and therefore is connected to a thermocouple. The other one is the device under test, which has to be aligned to the centre of the chamber. The sample for temperature measurements is placed next to it. The chamber is heated up using infrared lamps placed underneath the sample station. Communication with the measurement PC takes place via command files. In this way

the desired heating rate can be set. For this thesis a heating rate of 6 K per minute was used. For determination of wafer curvature there is a grid consisting of twelve laser points directed at the device under test. When the sample starts to bow due to the different thermal expansion of copper and silicon, the curvature can be calculated from the deviation of the reflected beams from initial position. Although there was no interest in measuring the curvature of our diodes, it was important to align the laser beams on a dummy sample when annealing the diodes, otherwise the measurement program was aborted. Before starting the heating ramp, the measurement chamber was evacuated and afterwards nitrogen was let in to avoid oxidation. The waferbow measurement station does not have an active cooling therefore the cool down is subject to the thermal properties of the furnace itself.

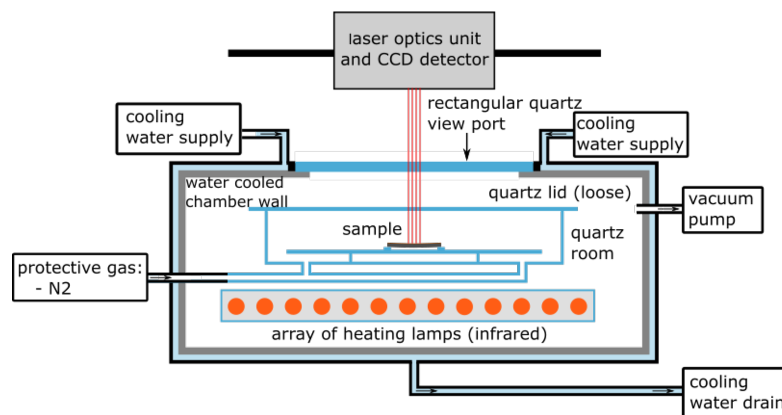

Figure 5.3: Schematic representation of the waferbow measurement station used for annealing experiments.

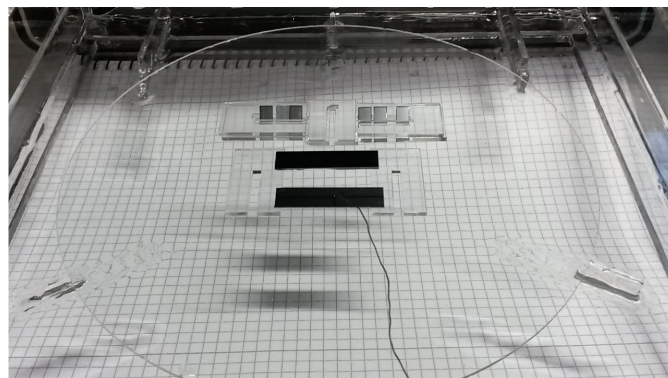

Figure 5.4: Sample station within the waferbow measurement tool. All the samples are put onto a quartz wafer. Six pn-diodes are placed within quartz sample holders so that they are not moved by the N_2 gas flow (top). In the middle there are two Cu coated Si wafer pieces, one for curvature measurement (middle) and one for temperature measurement (bottom), which is linked to the thermocouple (wire).

6 Investigated samples

The test structures investigated are p^+/n Si diodes fabricated from floatzone Si with a phosphorus doping concentrations ranging from $1 \cdot 10^{13}\ \mathrm{cm}^{-3}$ to $3 \cdot 10^{14}\ \mathrm{cm}^{-3}$. The samples are provided from Infineon Technologies Austria AG, Villach. All diodes contain Pt which acts as minority-carrier lifetime killer. It is brought into the Si via vapour deposition and is diffused in at high temperatures. The main investigations were carried out on two nearly identical 400 V class diodes (A and B) with edge termination. They underwent the exact same processing steps and experienced the same thermal budget.

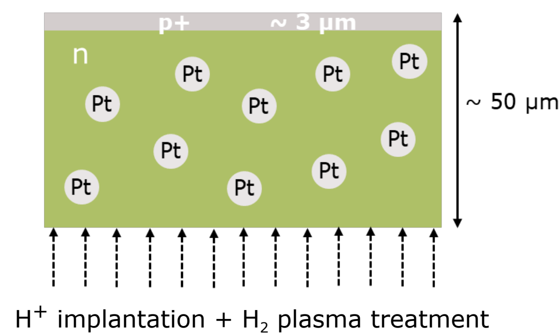

Figure 6.1: Schematic representation of the diode test structures (A and B) investigated. The H^+ implantation is only performed on Sample A to introduce the field-stop zone. Back and front metallization are not shown in this drawing for simplicity reasons.

The only difference between sample A and B is the field-stop which is present only in sample A. The field-stop zone is brought in via implantation of protons from the backside of the diode with two implantation energies and proton doses leading to two doping peaks. According to the experimental plan the peaks are expected to be in depths of approximately 4 and 16 µm (from backside). Reference measurements were performed on a 3.3 kV class diode without field-stop (sample C).

Tab. I contains detailed information about the different diodes investigated.

Table I: Overview of Si p^{+}/n-diodes investigated

Sample	**A**	**B**	**C**
Break-down Voltage			
480 V	X	X	
3.3 kV			X
Phosphorus doping concentration			
$1 \cdot 10^{13}$ cm^{-3}			X
$3 \cdot 10^{14}$ cm^{-3}	X	X	
Effective area			
0.46 cm^2	X	X	
0.91 cm^2			X
Wafer thickness			
50 µm	X	X	
450 µm			X
Field-stop (proton implanted)	X		

7 Experimental results

The content of this chapter will be published in the International Semiconductor Conference Proceedings 2018 available on the IEEE Xplore Digital Library.

7.1 Motivation

In this chapter the electrically active defects in Si p^+/n diodes with Pt doping for minority-carrier lifetime control are investigated. Trap concentrations, their position within the Si band-gap as well as their influence on the diode performance are of high interest. In addition, the effect of field-stop zones introduced by ion implantation on the defects shall be investigated. The utilized electrical characterization techniques are IV- and CV-measurements whereas it is tried to establish a connection between these data and the defect information obtained from DLTS. Finally, the influence of annealing on defect concentration and the implanted field-stop is examined.

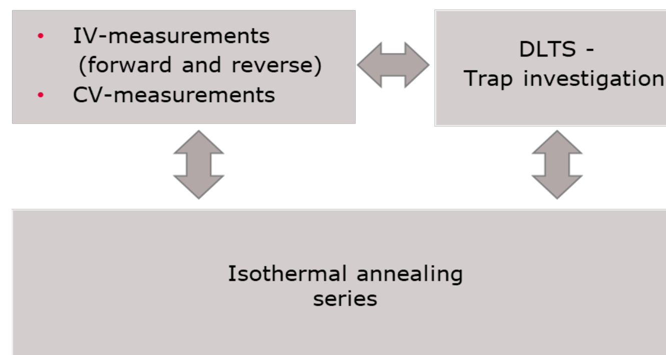

Figure 7.1: Methods used for defect investigation. Finding the interconnection between results from different measurements is a main aim.

7.2 Diode characteristics in forward and reverse operation

To get a first overview of the device performance of the different diodes electrical characterization measurements like CV- and IV-measurements were performed. IV curves of diode A and B are depicted in Fig. 7.2.

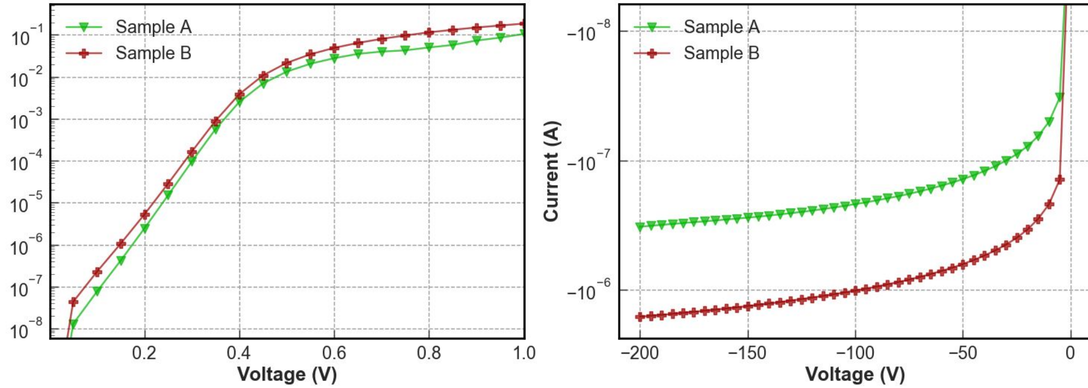

Figure 7.2: Forward (left) and reverse current characteristics (right) of two similar p^+/n diodes. Sample A has a field-stop zone produced by proton implantation which is missing in sample B.

The current diode characteristics of sample A and B already show significant differences. While the curves show a different slope of the exponential part in forward operation, the reverse current of sample A is about half an order of magnitude smaller than the one of sample B. The fact that the leakage current varies with applied bias indicates the domination of the generation current I_{gen} over the ideal diffusion current I_{diff} [30]. To quantitatively describe the different forward currents, the non-ideality factor η was calculated from the Schockley diode equation 4.19 for voltages obeying $qV \gg kT$. It was found that sample A has a lower non-ideality factor and therefore shows more ideal behaviour than sample B (see Tab. II). The reverse current at 50 V was found to be four times higher in the diode without field-stop (Sample B).

Table II: Diode performance parameters extracted from forward characteristic

Quantity	**Sample A**	**Sample B**
Non-ideality factor η	1.10	1.18
Reverse current I_R **at 50 V [µA]**	14	63

7.3 High-voltage CV measurements

As a next step the CV curves of sample A and B were measured. Up to an applied bias voltage of 40 V there is no difference detectable which is not surprising since only depths up to about 10 μm from pn-junction are investigated which is far from the field stop zone. A CV measurement setup including a bias-tee allowed for an increase of applied bias without destroying the CV meter. The voltage was swept from 0 V up to the break-down voltage of the diodes (~ -500 V) using variable step sizes. To gain the maximum of information from the data a donor concentration depth profile was calculated as described in 4.2 using Eq. 4.16 for depth calculation and Eq. 4.18 to obtain the corresponding donor concentrations.

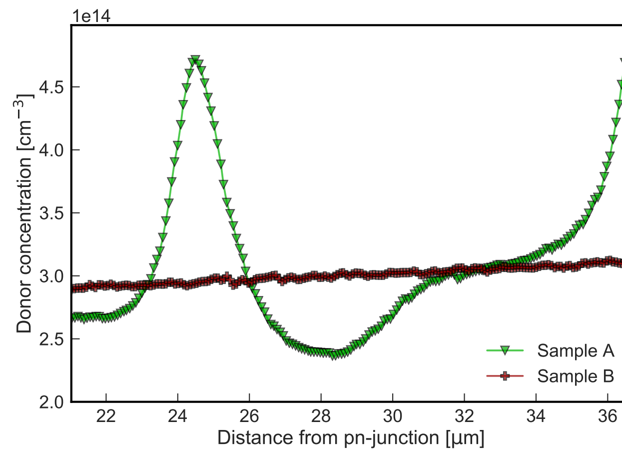

Figure 7.3: Donor concentration depth profile of p^+/n junctions with (sample A) and without field-stop (sample B).

The donor concentration within the field-stop zone shown in Fig. 7.3 was calculated from the high-voltage CV-curve. To reach the depicted depth range voltages between -200 and -500 V were necessary. Sample B shows a dopant concentration which is about constant around $3 \cdot 10^{14}$ cm^{-3} throughout the whole investigated depth range. The profile of sample A reveals a very pronounced peak at a distance of 25 μm from pn-junction which is most probably one of the peaks caused by proton implantation. It is well-known that the implantation of protons can create hydrogen-related donors in this zone which form the field-stop [7, 23, 35]. At 28 μm the concentration reaches a minimum until it returns to equilibrium concentration at 31 μm. At the end of the measurable range the number of donors seems to sharply increase again. This could either be due to the second field-stop peak or a measurement artefact since the break-down voltage of the diode is reached. To obtain the depth-profile within the entire field-stop zone with CV-measurements one could try to thin the diode beginning from the p-side and then forming a Schottky-contact, but this would be rather difficult since the diode

already has a thickness of only about 50 µm. Another option is the investigation of diodes with a lower base doping concentration so that the depletion width penetrates further into the material at lower voltages.

7.4 Separation of leakage current components

As already described in Chapter 4.3, the combination of the reverse current characteristic with the CV-curve of the same junction can provide useful information about important devices properties. By graphical representing Eq. 4.20 one can not only separate the saturation diffusion current I_{diff} from generation current I_{gen} but one can also calculate the generation lifetime τ_{g} which may contain information about electrically active defects. One has to consider that the separation technique only gives plausible results for rather small reverse bias voltages up to around 5 V. Experimental data are shown in Fig. 7.4.

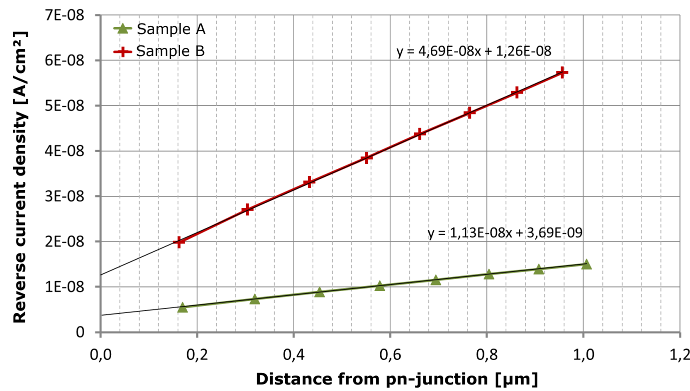

Figure 7.4: Separation method after Murakami and Shingyouji [22]: The intersection with the y-axis gives I_{gen} while the generation lifetime can be extracted from the slope.

From Fig. 7.4 it is obvious that the generation current I_{gen} of sample A is significantly smaller than the one of sample B. This is in accordance with the much higher reverse current of sample B. The exact calculated values are listed in Tab. III.

Table III: Values obtained from separation method

Quantity	Sample A	Sample B
Generation lifetime τ_{g} [µs]	20.5	3.7
Diffusion current density J_{diff} [nA cm^{-2}]	5.0	12.6
Diffusion current I_{diff} [nA]	2.3	5.8

Having a closer look at the saturation value of the diffusion current shows that it makes up only about one percent of the total reverse diode current which is in the range of 10^{-7} A. This confirms the above-mentioned statement that the leakage current is dominated by the generation current.
The connection of τ_g with the trap level position within the band-gap can be expressed as [30]

$$\tau_g = 2\tau_r \cosh\left(\frac{E_T - E_i}{kT}\right) \tag{7.1}$$

with the Fermi level position of the intrinsic semiconductor E_i which is $\sim E_G/2$. In principle, that would allow to derive the trap level position with respect to mid-gap, under the condition that $E_T \neq E_i$. Unfortunately, a lot of metal and transition metal defects (or defect complexes) cause trap levels near the middle of the Si band gap which makes it impossible to determine their position from Eq. 7.1. For that reason other methods like DLTS must be taken in consideration for defect identification.

7.5 Defect identification with DLTS

To correlate the measured device performance with information about defect levels within the band gap, the samples were investigated by DLTS. Spectra of both p^+/n Si diodes were recorded applying a filling pulse V_f of 1 V forward bias for 10 ms. As mentioned above, pulse durations longer than 1 ms were found to be sufficient to reach complete filling of (majority carrier) traps and thus a saturation of the MCTS signal. The forward bias filling pulse was chosen to include majority as well as minority (at least qualitatively) carrier traps in the measurement (MCTS). The recovery pulse V_r of -9 V is applied for 100 ms.

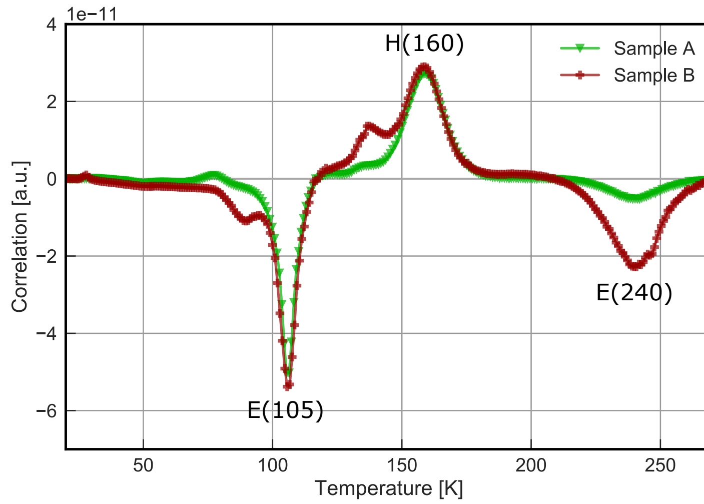

Figure 7.5: MCTS spectra of the two investigated samples. The signal is calculated using a rectangular correlation function.

The MCTS spectra in Fig. 7.5 show three significant peaks in both p^+/n diodes. Two majority carrier (electron) trap peaks (negative sign) at 105 K and 240 K as well as one minority carrier (hole) trap peak (positive sign) at 160 K. In the following the traps are termed using the defect type and the temperature of the DLTS peak maximum e.g. E(105) meaning the electron trap peak at 105 K.

The most significant difference between the two samples is the height of the E(240) peak which means that the amount of the corresponding defect is much lower in sample A. Furthermore there are two "shoulders" visible at the H(160) as well as at the E(105) peak which are likely to be other higher order Pt-H defects only present in sample B.

Attempts to identify the traps were made by calculating their energy level E_{T} within the band gap and comparing the values to literature. Also the mean trap concentration N_{T} and an approximate capture cross σ section of the traps were calculated. Note that σ can hardly be determined very accurately and suffers from discrepancies which is why also the values listed in literature often differ by orders of magnitudes. The values obtained are listed in Tab. IV.

Table IV: Trap parameters determined from Arrhenius analysis of the DLTS data

Property	**E(105)**	**H(160)**	**E(240)**
$E_\mathbf{T}$ **[eV]**	$E_\mathrm{C} - 0.23$	$E_\mathrm{V} + 0.36$	$E_\mathrm{C} - 0.50$
$\sigma_\mathbf{n}$ **or** $\sigma_\mathbf{p}$ **[cm^2]**	$5 \cdot 10^{-15}$	$2 \cdot 10^{-15}$	$2 \cdot 10^{-16}$
$N_\mathbf{T}$ **[cm^{-3}]** **Sample A**	$> 0.1 \cdot N_\mathrm{D}$	$9.6 \cdot 10^{12}$	$1.6 \cdot 10^{12}$
$N_\mathbf{T}$ **[cm^{-3}]** **Sample B**	$> 0.1 \cdot N_\mathrm{D}$	$1.0 \cdot 10^{13}$	$7.0 \cdot 10^{12}$
Assignment	Pt (substitutional)	Pt (substitutional)	Pt-H
Reference	$E_\mathrm{C} - 0.23$ [4, 20]	$E_\mathrm{V} + 0.36, E_\mathrm{V} + 0.32$ [15, 4]	$E_\mathrm{C} - 0.50$ [27]

Since it is known from the experimental plan that the diodes contain Pt the E(105) and H(160) peaks with trap levels of $E_\mathrm{C} - 0.23$ eV and $E_\mathrm{V} + 0.36$ eV respectively, can be assigned to platinum atoms occupying substitutional sites of the Si lattice with high certainty. Since its amount is higher than $0.1 \cdot N_\mathrm{D}$ the approximation made in Eq. 4.5 is not valid anymore, therefore an exact determination of trap concentration is not measurable with the conventional DLTS method. In literature $0.1 \cdot N_\mathrm{D}$ is in general stated as upper detection limit of DLTS [29].

The identification of the level $E_\mathrm{C} - 50$ eV is not unambiguous. Although it is reported for many years, its assignment is controversal and there exist several theories about which defect is responsible for this level [13]. Suggestions are Pt-Pt pairs [9, 33], Pt-O complexes [15, 10, 14], Pt-vacancy defects and Pt-H complexes, as proposed by Sachse et al. [27].

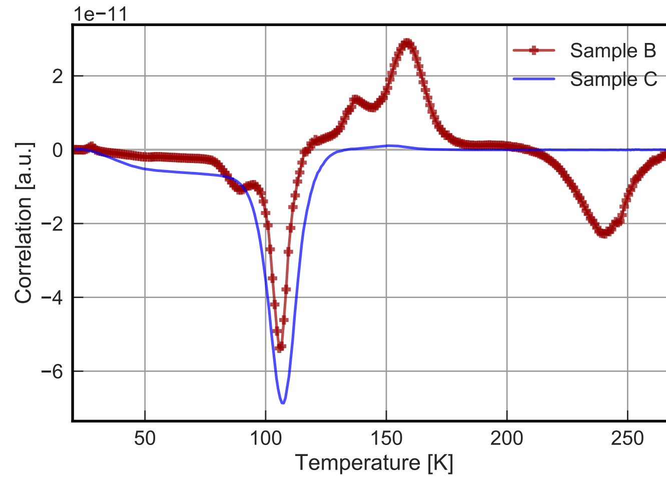

Figure 7.6: MCTS spectra of p^+/n diodes: Sample B is exposed to H_2 in a plasma treatment step, which is suspected to cause the E(240) defect. Platinum (E(105) and H(160)) is present in both samples.

However, sample A and B are exposed to hydrogen during a H_2 plasma treatment processing step. The comparison with DLTS spectra of sample C, which is similar in production to the other samples but does not undergo the hydrogen plasma treatment shows, that the E(240) peak is completely missing (see Fig. 7.6). Therefore the assumption is made that this level is caused by a defect involving hydrogen as already suggested by Sachse et al. [27], most likely Pt-H. Taking into account that the energy level of the E(240) defect lies close to the middle of the Si band-gap, this defect can be an explanation for the high leakage current in reverse as well as for the higher non-ideality factor η in forward operation.
It is also conspicuous that the H(150) peak is only very weakly pronounced in sample C.

7.6 Calculation of defect profiles from reverse IV measurement

From monitoring the reverse current density gradient with respect to depletion width W (which corresponds to the distance x from pn-junction) dJ_{gen}/dx, information about the distribution of defect centres responsible for current generation can be obtained [8]. Given that the Shockley-Read-Hall theory is valid and that the dominant emission process is not field dependent due to the Pool-Frenkel effect [5], the derivative of J_{gen} with respect to W is directly proportional to the concentration of generation levels at the corresponding depth according to the relation

$$\frac{dJ_{\text{gen}}}{dx} = qN_{\text{T}}(x)\xi. \tag{7.2}$$

In Eq. 7.2 ξ is the emissivity. If there are several generation levels present, the sum of the products of the particular trap concentrations and emissivities has to be considered. But in general there is one defect level dominant, usually the one which is closest to the middle of the band-gap, so that the obtained depth profile corresponds to this certain defect. Thus, the profile depicted in Fig. 7.7 shows the development of the E(240) defect centre with depth. As already mentioned, since the generation current is the dominating component of the leakage current, the calculations were performed assuming $J_{\text{gen}} \approx J_{\text{R}}$. The emissivities for both samples were calculated using the mean trap concentrations within the depletion width at applied biases up to -9 V and the derivative of the reverse current density. The resulting emissivities for sample A and sample B are 486 s^{-1} and 470 s^{-1}, respectively.

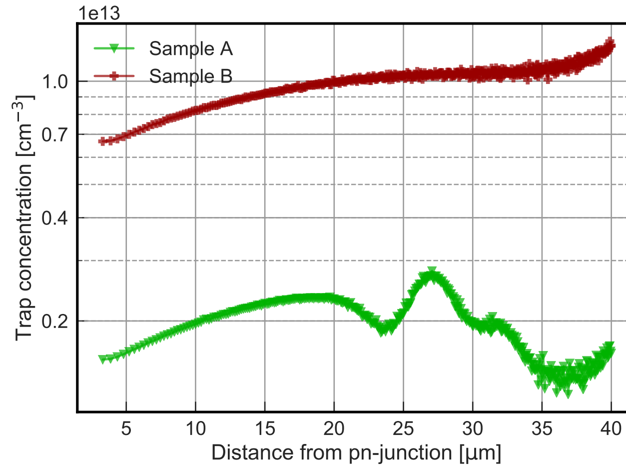

Figure 7.7: Depth profile of the E(240) defect center, which is closest to mid-gap, calculated from the IV characteristic in reverse operation.

Both samples show the same trend with respect to depth, a steady increase of the trap concentration up to a depth of 20 µm. Nevertheless, the absolute concentration of the E(240) defect is about four times lower throughout the whole range in sample A, as already evaluated with DLTS. However, this finding was a little bit surprising at first. It has been expected that the proton implantation leads to a higher number of hydrogen available for Pt-H formation, thus a higher Pt-H concentration in sample A with field-stop seemed logical. Considering the measurements results revealing the opposite, the conclusion is made that the proton implantation causes several kinds of vacancy complexes within the field-stop region, consuming hydrogen

introduced from the backside and tending to form hydrogen-related donors or other stable higher-order hydrogen related complexes. Thus, the number of hydrogen atoms available for Pt-H complex formation is reduced and this can lower the overall Pt-H defect concentration in Sample A in the drift region. The trap density in the diode without field-stop keeps increasing up to about 25 μm and then seems to reach a plateau around a concentration of $1 \cdot 10^{13}$ cm^{-3}. Approaching the surface the E(240) concentration seems to further increase again. A possible explanation would be the assumption, that the density of Pt-H defects results from the superimposition of the U-shaped Pt-profile (as described in 3) with the number of H atoms which decreases approaching the pn-junction since the H_2 plasma treatment is performed on the back-side of the diode.
The defect concentration in sample B clearly shows two minima at 24 μm and 36 μm. This behaviour is attributed to the proton implanted field-stop which influences the donor concentration and so the validity of this method. The distance from pn-junction is calculated using Eq. 4.13 assuming a constant doping concentration throughout the whole depth range, which is not the case in the field-stop region. So it is likely that, since the actual donor concentration is higher in the field-stop zone, this leads to an underestimation of the Pt-H trap concentration and therefore causes the minima in the depth profile. However, this does not affect the main finding, namely that the overall E(240) concentration is significantly lower in the diode with field-stop (sample A).

7.7 SRP results

To verify the above mentioned theory that the field-stop influences the E(240) defect concentration, its depth profile is compared to the measurement data obtained from SRP. This is shown in Fig. 7.8.

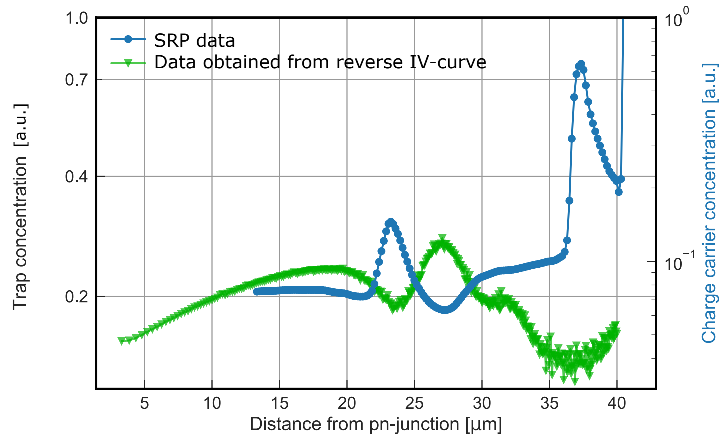

Figure 7.8: E(240) depth profile obtained from IV characteristics (green triangles) and charge carrier concentration measured with SRP (blue circles).

Superimposition of the calculated trap concentration profile with the charge carrier density obtained from SRP clearly shows that maxima in the E(250) curve always occur at the same position as minima in the SRP profile and vice versa. This confirms that there is a connection between field-stop and the mid-gap defect depth profile. However, it does not necessarily mean that the Pt-H concentration actually drops at the field-stop layers. As mentioned above it has to be considered that the calculated concentration values and also the distance from pn-junction in this region is not reliable, since for the evaluation a constant doping profile was assumed.

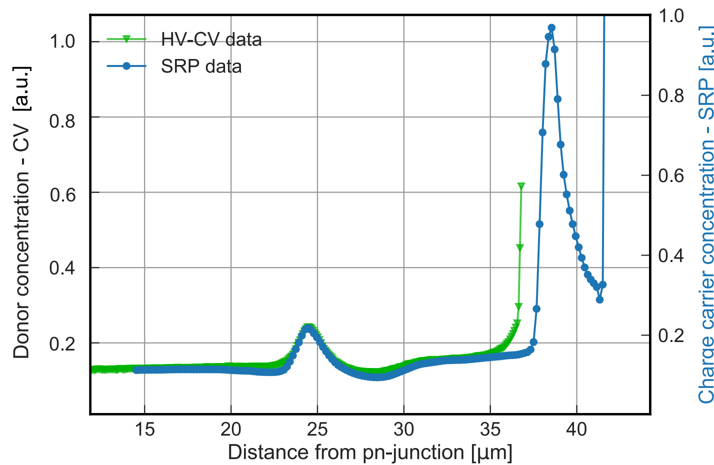

Figure 7.9: Donor concentration calculated from high voltage CV measurement (green triangles) and determined from SRP (blue circles).

The comparison of the donor concentration profile obtained from CV-measurement with the one compared from SRP is depicted in Fig. 7.9. The curves nearly perfectly overlap in the area of the field-stop peak which lies closer to the pn-junction. The second peak is shifted to the left in the CV obtained curve, but the rapid increase could again be due to the fact that the voltage exceeds break-down voltage in this range already. One has to note that the concentrations calculated from CV-measurement differ from the one determined with SRP. However, in this case the donor profile calculation from high voltage CV-measurements seems like a good alternative to SRP measurements. It is much less complicated, faster and gives as good qualitative results for the samples investigated in this thesis.

7.8 DLTS depth profiles

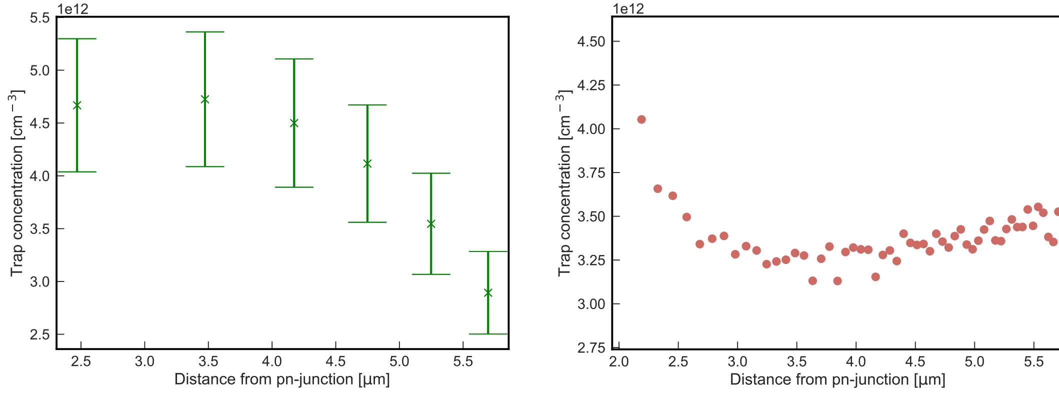

Figure 7.10: Pt-H depth profile of E(240) defect obtained with DLTS (left) and derivate of diffusion current (right).

Since the number of Pt-H defects is in the range of $10^{-2} \cdot N_D$ which should give good quantitative trap concentration results when investigated with DLTS, a depth profile of the defect was tried to be measured as described in Chapter 4.1.11. The obtained profile is depicted in Fig. 7.10 (left) and compared to the Pt-H profile calculated from the derivative of the generation current (right). The DLTS depth profile was measured by varying the filling pulse between 0 V and 6 V with a step width of 1 V while the recovery pulse was held constant at 9 V. The distance from pn-junction was calculated assuming a uniform doping concentration and considering the applied voltage, using Eq. 4.13 for both profiles. However, there are significant differences between theses two. While the DLTS profile starts decreasing slowly at depths larger than 3.5 µm, the concentration obtained from the reverse current increases rapidly up to depths

around 3 μm and then remains constant at a Pt-H density of about 3.5 $\cdot 10^{12}$ cm^{-3}. Only the calculated defect concentration is about the same for both methods.

As an attempt to explain the discrepancies the sensitivity for both depth profiling methods was calculated. Considering the profile obtained from the derivative of leakage current after [8], the sensitivity was estimated from

$$\delta N_\mathrm{T} = \frac{1}{q\xi}\frac{\delta J_\mathrm{gen}}{\delta x} \tag{7.3}$$

where δJ_gen is the minimal detectable change of the current density and δx is defined as the transition region between space-charge region and neutral semiconductor which is approximately three times the extrinsic Debye-length which is expressed as

$$\lambda_\mathrm{ex} = \sqrt{\frac{\epsilon k T}{q^2 N_\mathrm{T}}}. \tag{7.4}$$

For the pn diode test structures investigated in this thesis with an n-doping concentration of $3 \cdot 10^{14}$ cm^{-3} ($\lambda_\mathrm{ex} \approx 400$ nm) and a minimal detectable leakage current density $\delta\ J_\mathrm{gen} = 2$ pA/cm^{-3} the attainable resolution gives $\delta N_\mathrm{T} \approx 3 \cdot 10^{10}$ cm^{-3}.

For DLTS depth profiling the sensibility was estimated from Eq. 4.6, yielding an attainable resolution of $\delta N_\mathrm{T} \approx 2 \cdot 10^{10}$ cm^{-3}, which is in the same order of magnitude as the one calculated for the leakage current method. Also the depth resolution can be assumed similar, since also in DLTS the spatial resolution is limited by the transition region from depletion layer to neutral semiconductor and can therefore be assumed as $\approx 3\lambda_\mathrm{ex}$. However, from these results it can be concluded that the differences in the profiles obtained are not due to a resolution limit reached with one of the methods.

7.9 Annealing experiments

To gain further information about the supposed Pt-H defect complex, isothermal annealing experiments were performed. To begin with, appropriate experimental conditions such as annealing time t_ann and temperature T_ann had to be estimated. According to literature , the Pt-H pair is the most stable defect among the defect complexes formed between Pt and H with dissociation taking place at temperatures larger than 600 K [27, 28]. Another source states that annealing at 377°C for one hour is sufficient to cause the dissociation of Pt-H [2]. Therefore the choice of the annealing parameters was oriented towards these values. As first estimation, the Pt-H concentration was determined from leakage current as already described in 7.6, afterwards the calculated defect density was compared to values obtained by DLTS. Several

electrical characterizations of the diodes were performed before and after each annealing step. The sequence of measurements is shown below.

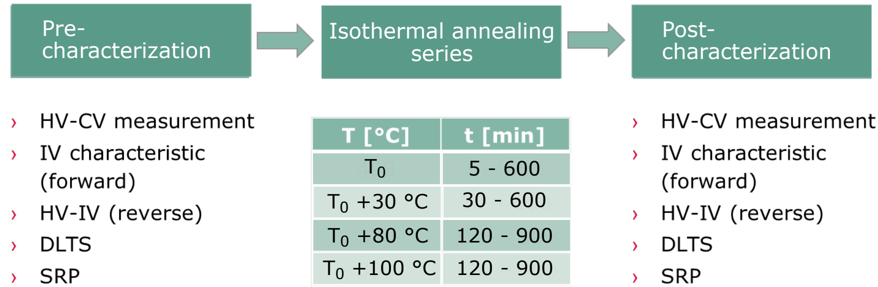

Figure 7.11: Annealing procedure: Electrical characterizations are carried out before and after each annealing step.

7.9.1 DLTS spectra after annealing

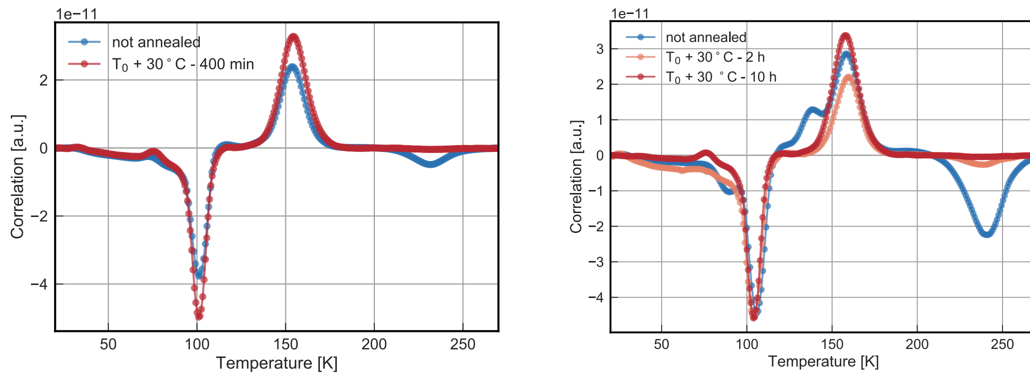

Figure 7.12: MCTS spectra of the diode with (left) and without field-stop (right) before and after annealing at $T_0 + 30°\text{C}$.

Fig. 7.12 shows the MCTS spectra before and after annealing at $T_0 + 30°\text{C}$ for two and ten hours respectively. The most striking difference after the first annealing step is the reduction of the E(240) peak intensity corresponding to a decrease in Pt-H concentration. Furthermore the shoulder at the low temperature side of the H(160) peak disappeared and the H(160) peak hight itself is lowered while the E(105) peak remains approximately the same. Assuming that Pt-H dissociates to Pt and H during the annealing step, it was expected that the peaks assigned to Pt (E(105) and H(160)) increase while the E(240) decreases.

Table V: Trap concentrations determined after annealing at $T_0 + 30°C$

Sample A	E(105)	H(160)	E(240)
not annealed	$5 \cdot 10^{13}$	$1 \cdot 10^{13}$	$7.8 \cdot 10^{12}$
2 h	$5.2 \cdot 10^{13}$	$8.6 \cdot 10^{12}$	$1.0 \cdot 10^{12}$
10 h	$5.9 \cdot 10^{13}$	$1.0 \cdot 10^{12}$	$1.5 \cdot 10^{11}$

Sample B	E(105)	H(160)	E(240)
not annealed	$4.3 \cdot 10^{13}$	$9.5 \cdot 10^{12}$	$1.6 \cdot 10^{12}$
10 h	$4.6 \cdot 10^{13}$	$1.1 \cdot 10^{13}$	$2.5 \cdot 10^{11}$

The individual calculated trap concentrations are listed in Tab. V. There is a slight increase in the E(105), but it is not known how exact this result is since the trap density is already $> 0.1\ N_D$ which is the upper limit for reliable concentration determination in DLTS. The H(160) peak on the other hand, seems to decrease in sample B without field-stop due to the annealing while it increases slightly in sample A. The shoulder at the H(160) low temperature side could give an explanation for this difference. It is suggested that there is another DLTS peak, probably corresponding to a defect also including Pt and H, overlapping with the H(160) peak. As the sample gets annealed, this defect dissociates which makes it look like the H(160) peak decreases. At this point it has to be pointed out that the obtained H(160) trap densities are not very reliable as well, since it is a hole trap within n-type material, which means that it is not known if the forward voltage injection pulse is sufficient to even fill all of the existing traps. To summarize, the only concentration to be reliably determined is the number of E(240) traps, while the other two peaks solely give a rough quantitative estimation and a proof of the presence of these levels.

7.9.2 Influence on reverse current

Since the E(240) level lies approximately in the middle of the Si band gap it is expected to provide the main contribution to generation current [18]. The dissociation of this Pt-H defect due to annealing should therefore be detectable by a reduction of the reverse current I_R.

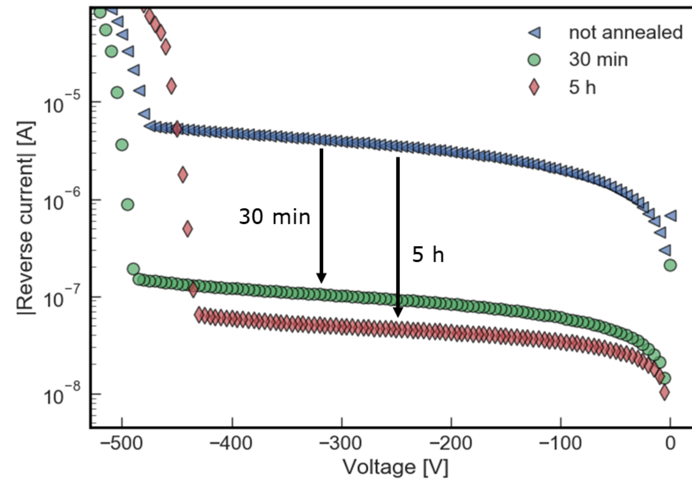

Figure 7.13: Annealing at $T_0 + 100°C$ causes a rapid decrease in leakage current.

Fig. 7.13 shows the monitored IV-characteristics in reverse operation for the first annealing series at $T_{ann} = T_0 + 100°C$. An annealing step of only 30 min already caused a reduction of leakage current of nearly two orders of magnitude. Increasing the duration of the heat treatment to 5 hours leads to a further slight reduction. The sample depicted here is the one without field-stop (sample B). The same trend can also observed for sample A and for annealing series at lower T_{ann} but the decrease in leakage current is of course not that pronounced for lower temperatures. These findings suggest a strong reduction of Pt-H defects either by dissociation to Pt and H or by forming other defect complexes with e.g. vacancies, oxygen or carbon impurities which are electrically inactive.

7.9.3 Determination of dissociation energy

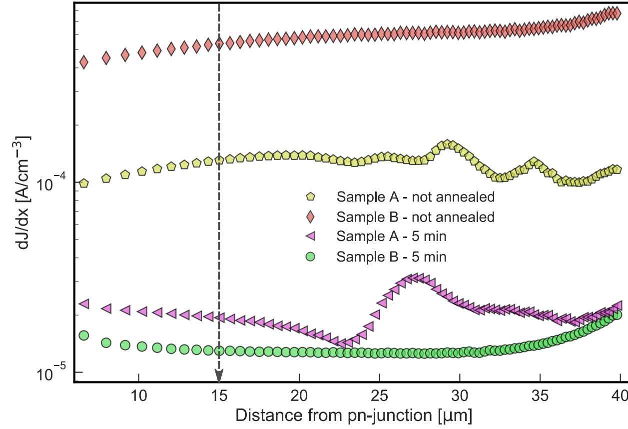

Figure 7.14: $\mathrm{d}J_\mathrm{R}/\mathrm{d}x$ vs distance from pn-junction to determine the E(240) complex depth profile before and after annealing at $T_0 + 100°\mathrm{C}$ for five minutes. The trap concentration is evaluated at a depth of 15 µm.

Having a look on the Pt-H depth profiles in Fig. 7.14 clearly shows a rapid overall reduction of the defect throughout the whole sample in both diodes. While the trap concentration is reduced by more than an order of magnitude in the sample without field-stop, the defect concentration in the sample with field-stop still decreases by approximately 0.9 orders of magnitude. It is notable that the end-concentration in sample A is higher although it has a lower Pt-H concentration to begin with. In sample A the two field-stop peaks seem to diffuse out during annealing, leaving one large Pt-H peak at 26 µm and a slightly increased base concentration at the backside of the diode. For further investigation the trap concentration was evaluated at a depth of 15 µm from pn-junction, where the Pt-H concentration can be assumed approximately constant but the field-stop zone is not yet reached. This allows a comparable evaluation of the defect concentration development since complex processes within the field-stop are not considered. Fig. 7.15 shows the measured Pt-H concentrations for two different isothermal annealing series.

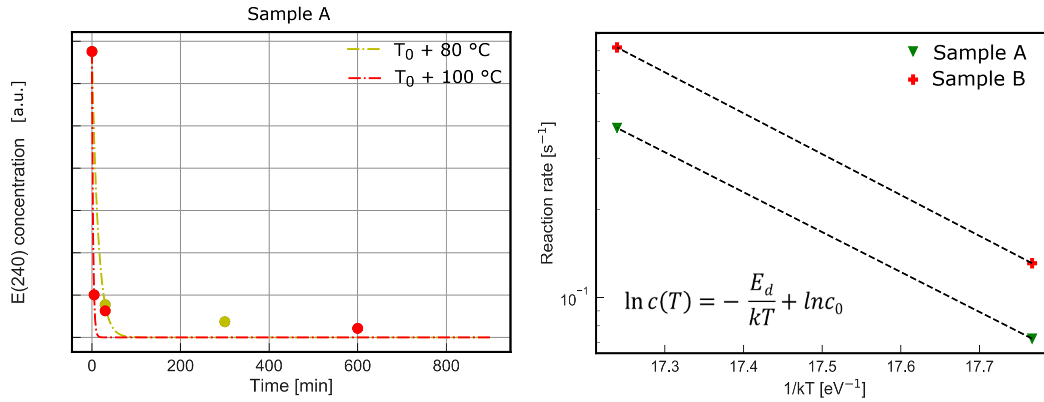

Figure 7.15: Left: development of E(240) defect concentration during isothermal annealing at $T_0 + 80°\text{C}$ (yellow) and $T_0 + 100°\text{C}$ (red). Right: Arrhenius plot of the first two annealing series for a first estimation of E_d.

The annealing curve above shows that the Pt-H defect concentration increases rapidly within the very first minutes of the annealing process and reaches a plateau in the range of $5 \cdot 10^{10}$. Obviously the chosen temperatures are too high so that a slower exponential decrease of the curve is not resolvable. That is why the first two annealing series were used to pre-estimate the dissociation energy E_d and reaction rate constant c_0 as described in 4.5 and simulate annealing series at lower temperatures. From this, more suitable measurement parameters were determined. The pre-estimated values are an dissociation energy E_d of 2.1 eV and a reaction rate constant c_0 of $2.3 \cdot 10^{10}\ \text{s}^{-1}$.
The resulting simulated annealing curves are depicted below. From Fig. 7.16, $T_0 + 30°\text{C}$ and T_0 were determined as further annealing temperatures T_ann.

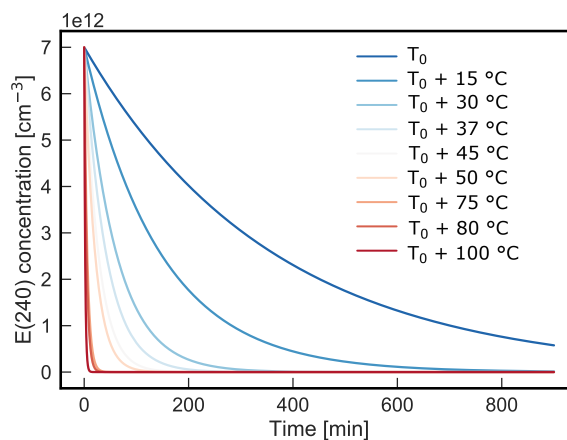

Figure 7.16: Simulated development of E(240) defect concentration upon isothermal annealing at different temperatures. The parameters E_d and c_0 are extracted from annealing measurements at $T_0 + 100°\text{C}$ and $T_0 + 80°\text{C}$.

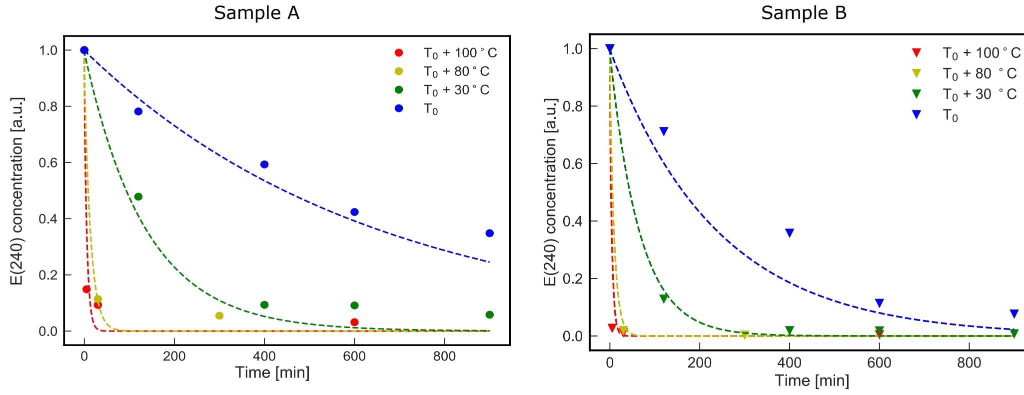

Figure 7.17: Isothermal annealing series for temperatures ranging from T_0 to $T_0 + 100°C$.

All performed isothermal annealing series are depicted in Fig. 7.17. The concentration decreases more slowly at lower temperatures, nevertheless the process does not show perfect exponential behaviour. This is especially visible by plotting the data semi-logarithmically (Fig. 7.18 (a)). Several attempts were made to find a possible explanation. As a first guess the generalized simple thermal (GST) model for thermal dissociation kinetics, as described by [31], was applied to the measurement data. This model assumes a spread of the dissociation energy E_d, following a Gaussian distribution in E_d with standard deviation σ_{ed} giving the generalized dissociation equation as

$$[A] = \frac{[A_0]}{\sqrt{2\pi}\sigma_{ed}} \int_{E_d - 3\sigma_{ed}}^{E_d + 3\sigma_{ed}} \exp - \frac{(x - E_d)^2}{2\sigma_{ed}} \times \exp\left[-tc_0 \exp\left(-\frac{x}{kT}\right)\right] dx. \tag{7.5}$$

However, this model is rather valid in amorphous materials and thus does not give a better fit or remarkable different results in this case of crystalline silicon.

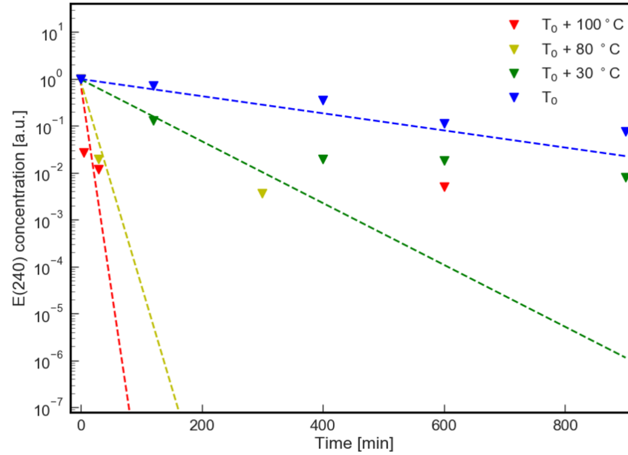

Figure 7.18: Annealing series of the sample without field-stop, logarithmic y-axis (a). Final Arrhenius plot for determination of the dissociation energy E_d (b)

.

It has to be considered that the annealing is not started at $t = 0$ at the temperature T_{ann} but that the heating happens quite slowly, in this case with a heating ramp of 6 K/minute. Also the cool-down phase (~ 5 K/min) adds to the total thermal budget to which the sample is exposed to during the single annealing steps. This means that the measured defect concentrations at high temperatures T_{ann} and short times t_{ann} are strongly affected by the heating and cooling ramp as well. This impact is thought to push these measurement points to concentration values lower than they would be under ideal measurement conditions, thus causing that "kink" to the right in the semi-logarithmic plot (see Fig. 7.18 (a)). It can also be seen that the measurement data do not diverge that much from ideal exponential behaviour at lower temperature. However, implementing the heat-up and cool-down phase in the curve-fitting algorithm showed that also this explanation is not sufficient to explain the observed severe deviations from exponential behaviour. The dashed lines in Fig. 7.17 and Fig. 7.18 (a) are the calculated fitting curves already taking into account the complete annealing $T - t$ curve including heat up and cool down. Another possibility could be that an equilibrium concentration of Pt-H in Si is reached at about $10^{-2} \cdot [\text{Pt-H}]_0$ within the investigated temperature range, explaining the kink in the concentration curves in Fig. 7.18 (a).

Comparison with annealing experiments in literature showed that these experiments are usually performed considering concentration variations of maximal one order of magnitude. Performing annealing series at lower temperatures and longer times is therefore expected to give better results.

The parameters obtained describing the Pt-H level dissociation process are

$$E_{\mathrm{d,\,w/\,FS}} = (1.5 \pm 0.4)\ \mathrm{eV} \qquad c_{0,\,\mathrm{w/\,FS}} = 2 \times 10^{8\pm1}\ \mathrm{s}^{-1}.$$

$$E_{\mathrm{d,\,w/o\,FS}} = (1.2 \pm 0.5)\ \mathrm{eV} \qquad c_{0,\,\mathrm{w/o\,FS}} = 3 \times 10^{7\pm1}\ \mathrm{s}^{-1}.$$

Since the calculated parameters shall describe the dissociation of the same defect level, it is not surprising that the values obtained for the diodes with and without field-stop are quite similar. The dissociation energy of the level in the diodes without field-stop lies within the error range of the energy calculated for the level in the diode with field-stop and vice versa. The same applies for the reaction rate constants. Since there were two differently processed diodes containing the same defect level with different starting concentrations investigated and both gave similar results describing the dissociation process, it is assumed that the model of a first order reaction applies in good approximation.

Unfortunately there were not found a lot of literature values about the dissociation of Pt-H complexes in Si to compare the experimental data with. The dissociation energy of an isolated Pt-H molecule is given in [19] as 330 kJ/mol corresponding to 3.4 eV which would be way higher than the calculated value. Another source [24] states the dissociation energy of "hydrogen passivated Pt" as $E_\mathrm{d} = 2.3$ eV, which is still not really close to the value extracted from the measurement data, but it is also mentioned that they assume the reaction rate c_0 in the range $10^{13} - 10^{14}\ \mathrm{s}^{-1}$.
According to [18] a value of c_0 on the order $10^{13}\ \mathrm{s}^{-1}$ or larger is an indicator of dissociation as dominating first order process. The small value of $2{\cdot}10^{8}\ \mathrm{s}^{-1}$ obtained in this case therefore indicates a large contribution of other processes such as diffusion limited reactions to form variations of other defect complexes, including for example oxygen, carbon and vacancies, which are not electrically active.

7.10 Connection between trap concentration and derivative of reverse current

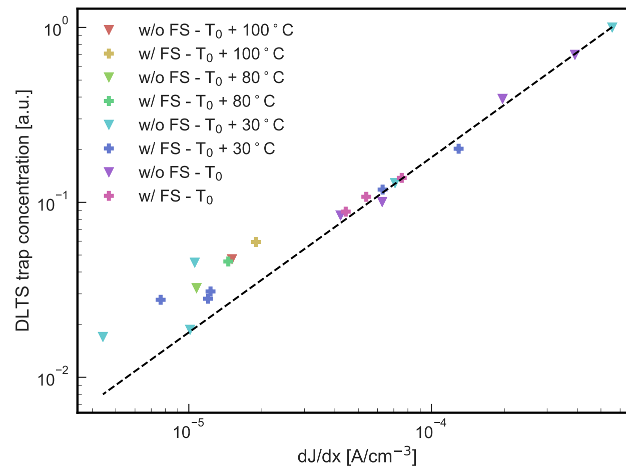

Figure 7.19: DLTS trap concentration vs. derivative of leakage current

Fig. 7.19 shows the mean Pt-H trap concentration determined with DLTS plotted over the derivative of the reverse current. The two quantities show a nice linear behaviour over the whole annealing time and temperature range and no matter if there is a field-stop present in the sample or not. This confirms the validity of Eq. 7.2 and proofs that the mid-gap E(240) level is the main contributor to the generation current. It is noticeable that points at lower defect concentration show a stronger deviation from linear behaviour. A possible explanation for this is the noise in the DLTS signal, which at concentrations $< 10^{-2} \cdot N_D$ can account for an overestimation of trap concentration of at least 30 %.

8 Conclusion and Outlook

Nowadays platinum is often introduced in silicon diodes which are used for applications where it is necessary to switch from conducting to blocking state very often and at high frequencies. Platinum creates two discrete defect levels within the silicon bandgap, one 0.23 eV below conduction band and another one 0.36 eV above the valence band. These two states enhance recombination while not producing high leakage current via generation, thus decreasing minority carrier life-time and make fast switching with low power losses possible. However, if Si diodes containing Pt are exposed to hydrogen, the Pt is very likely to form Pt-H complexes. These Pt-H defects were the main focus in this thesis. Their influence on diode performance, as well as their temperature stability was investigated. Furthermore the influence of proton implantation, as often used for field-stop zone formation, upon the Pt-H concentration was examined. The following conclusions were made:

- Pt-H complexes in Si cause an electron trap level 0.50 eV below the conduction band. Since this is very close to the middle of the Si bandgap, this defect acts as efficient generation centre. Diodes with Pt-H complexes thus have higher leakage currents than diodes containing only Pt.

- Proton implantation causes damage within the Si lattice such as vacancies, interstitials and vacancy complexes. These defects catch hydrogen to form hydrogen related shallow-donors, leaving less hydrogen available for Pt-H formation. By implanting protons from the backside it is therefore possible to influence the overall Pt-H concentration in the device.

- The Pt-H level is not thermally stable at elevated temperatures. It could be shown that annealing at T > $300°C$ leads to dissociation of the corresponding trap level and a significant reduction of leakage current. This does not necessarily mean that Pt-H dissociates forming Pt and H but could also mean that it starts diffusing around, forming other defects with e.g. oxygen or vacancy-complexes which are not electrically active. The calculated activation energy for this process assuming a first order reaction was 1.4 eV. Since the reaction rate constant obtained is much smaller than 10^{14} s^{-1} mere dissociation of the Pt-H defect could be excluded.

Since it is not known to which extend the Pt-H defect is wanted, further investigation in this field is necessary. Although it acts as efficient recombination centre, the higher leakage current could cause detrimental effects during application. Further research would also be necessary to fully understand the processes taking place especially in the field-stop region during implantation but also during annealing. The field-stop zone should not be affected by the annealing process. If the leakage current can be reduced by exposing the sample to elevated temperatures, but at the same time the field-stop zone starts to spread out, this may lead to different problems.

List of Symbols

A	area (cm^2)
C	capacitance (F)
C_∞	steady-state capacitance (F)
c_0	reaction rate constant (s^{-1})
c_n	electron capture rate (cm^3/s)
c_p	hole capture rate (cm^3/s)
C_{srp}	correction factor in SRP measurements
E_A	= E_T, activation energy of the trap (eV)
E_C	conduction band edge (eV)
E_d	dissocitation energy (eV)
E_F	Fermi energy (eV)
E_G	semiconductor band gap (eV)
E_i	Fermi level for the intrinsic semiconductor (eV)
e_n	electron emission rate (s^{-1})
e_p	hole emission rate (s^{-1})
E_T	trap energy (eV)
E_V	valence band edge (eV)
ϵ_{Si}	permittivity of silicon (F/m)
h	hole density (cm^{-3})
I	current (A)
I_{diff}	saturation value of ideal diffusion current (A)
I_{gen}	generation current (A)
I_L	leakage current (A)
I_R	reverse current (A)
J_{diff}	saturation diffusion current density (A/cm^2)
J_{gen}	generation current density (A/cm^2)
J_R	reverse current density (A/cm^2)
k	Boltzmann's constant (8.62×10^{-5} eV/K)

λ	distance from space-charge region edge to the intercept of the trap level with the Fermi-level (cm)
μ_n	electron mobility (cm^2/Vs)
μ_p	hole mobility (cm^2/Vs)
n	electron density (cm^{-3})
N_A	acceptor concentration (cm^{-3})
N_C	effective density of states in the conduction band (cm^{-3})
N_D	donor concentration (cm^{-3})
n_i	intrinsic carrier concentration (cm^{-3})
N_T	total deep-level impurity density (cm^{-3})
n_T	deep-level trap density occupied by electrons (cm^{-3})
N_V	effective density of states in the valence band (cm^{-3})
p_T	deep level trap density occupied by holes (cm^{-3})
q	elementary charge (1.6×10^{-19} C)
R	resistance (Ω)
r	radius (cm)
R_c	contact resistance (Ω)
R_{meas}	measured resistance (Ω)
R_p	probe resistance
R_{sp}	spreading resistance (Ω)
ρ	resistivity (Ωcm)
$S(T)$	DLTS signal (a.u.)
σ	capture cross section (cm^2)
σ_{ed}	standard deviation of dissociation energy (eV)
σ_n	electron capture cross section (cm^2)
σ_p	hole capture cross section (cm^2)
T	temperature (K)
t	time (s)
T_{ann}	annealing temperature (°C)
t_{ann}	annealing time (s)
t_f	filling pulse time (s)
t_r	recovery pulse time (s)

τ	lifetime (s)
τ_c	$=1/e_n$ electron capture time constant (s)
τ_g	generation lifetime (s)
V_{bi}	built-in voltage (V)
V_f	filling pulse voltage (V)
V_{fwd}	forward voltage (V)
V_r	recovery pulse voltage (V)
v_{th}	thermal velocity (cm/s)
W	space-charge region width (cm)
$w(t)$	weighting function
W_R	space-charge region width during recovery pulse (cm)
x	depth or distance from pn-junction (cm or µm)

List of Tables

I Overview of Si p^+/n-diodes investigated 31

II Diode performance parameters extracted from forward characteristic 33

III Values obtained from separation method 35

IV Trap parameters determined from Arrhenius analysis of the DLTS data 38

V Trap concentrations determined after annealing at $T_0 + 30°C$ 46

List of Figures

2.1 Possible transitions between trap level and band egdes 4

3.1 Depth profile of platinum in silicon 6

4.1 DLTS principle 9
4.2 DLTS: Capacitance transient 10
4.3 DLTS: Capacitance transient at different temperatures 12
4.4 DLTS correlation functions 13
4.5 DLTS: Capacitance signal evaluated with different correlation functions 14
4.6 DLTS: influence of recovery time 15
4.7 DLTS: influence of filling pulse duration 16
4.8 MCTS spectrum 17
4.9 IDLTS: current response 18
4.10 DLTS: depth profiling 19
4.11 Donor concentration calculated from CV curve 20
4.12 Separation technique 22
4.13 SRP principle 23
4.14 SRP: spreading current 23
4.15 Annealing: temperature program 25

5.1 Cryogenic probe station 27
5.2 DLTS measurement setup 28
5.3 Waferbow measurement setup - schematic 29
5.4 Waferbow setup 29

6.1 Diode test structure 30

7.1 Methods used for defect investigation 32
7.2 Results: diode characteristics 33
7.3 Results: Donor concentration depth profile 34

7.4 Results: Separation method . . . 35
7.5 Results: MCTS spectra . . . 37
7.6 Results: MCTS spectra - diode without H_2 plasma treatment . . . 39
7.7 Results: E(240) depth profile . . . 40
7.8 Results: E(240) depth profile obtained from IV characteristics compared with SRP results . . . 42
7.9 Results: Donor profile calculated from CV measurement . . . 42
7.10 Pt-H depth profile of E(240) defect obtained with DLTS (left) and derivate of diffusion current (right). . . . 43
7.11 Results: Annealing procedure . . . 45
7.12 MCTS spectra of the diode with (left) and without field-stop (right) before and after annealing at $T_0 + 30°$C. . . . 45
7.13 Results: Reverse IV curve after annealing . . . 47
7.14 Result: Pt-H profile before and after annealing . . . 48
7.15 Results: Concentration development during annealing . . . 49
7.16 Results: Simulated E(240) defect concentration upon annealing . . . 49
7.17 Results: isothermal annealing series . . . 50
7.18 Results: annelaing series and final Arrhenius plot for activation energy determination . . . 51
7.19 DLTS trap concentration vs. derivative of leakage current . . . 53

Bibliography

[1] AREHART, A. R.: *Investigation of electrically active defects in GaN, AlGaN, and AlGaN/GaN high electron mobility transistors*, The Ohio State University, Diss., 2009

[2] BADR, E. ; PICHLER, P. ; SCHMIDT, G. : Deep Energy Levels of Platinum-Hydrogen Complexes in Silicon. In: *Solid State Phenomena* Bd. 205 Trans Tech Publ, 2014, S. 260–264

[3] BORSUK, J. ; SWANSON, R. : Current transient spectroscopy: A high-sensitivity DLTS system. In: *IEEE Transactions on electron devices* 27 (1980), Nr. 12, S. 2217–2225

[4] BROTHERTON, S. ; BRADLEY, P. ; BICKNELL, J. : Electrical properties of platinum in silicon. In: *Journal of Applied Physics* 50 (1979), Nr. 5, S. 3396–3403

[5] FRENKEL, J. : On pre-breakdown phenomena in insulators and electronic semiconductors. In: *Physical Review* 54 (1938), Nr. 8, S. 647

[6] GÖSELE, U. ; FRANK, W. ; SEEGER, A. : Mechanism and kinetics of the diffusion of gold in silicon. In: *Applied physics* 23 (1980), Nr. 4, S. 361–368

[7] HARTUNG, J. ; WEBER, J. : Shallow hydrogen-related donors in silicon. In: *Physical Review B* 48 (1993), Nr. 19, S. 14161

[8] HAZDRA, P. ; RUBEŠ, J. ; VOBECKỲ, J. : Divacancy profiles in MeV helium irradiated silicon from reverse I–V measurement. In: *Nuclear Instruments and Methods in Physics Research Section B: Beam Interactions with Materials and Atoms* 159 (1999), Nr. 4, S. 207–217

[9] HÖHNE, M. : Electron paramagnetic resonance of a platinum pair complex in silicon. In: *Physical Review B* 45 (1992), Nr. 11, S. 5883

[10] HÖHNE, M. ; JUDA, U. : Complexing of platinum in float zone and Czochralski silicon-electron paramagnetic resonance study of 6-platinum clusters and oxygen related 1-platinum midgap defect. In: *Materials science and technology* 11 (1995), Nr. 7, S. 680–683

[11] HOLM, R. ; HOLM, E. : *Electric contacts handbook*. Springer, 1958

[12] JELINEK, M. ; LAVEN, J. ; KIRNSTOETTER, S. ; SCHUSTEREDER, W. ; SCHULZE, H.-J. ; ROMMEL, M. ; FREY, L. : A DLTS study of hydrogen doped czochralski-grown silicon. In: *Nuclear Instruments and Methods in Physics Research Section B: Beam Interactions with Materials and Atoms* 365 (2015), S. 240–243

[13] JONES, R. ; RESENDE, A. ; OBERG, S. ; BRIDDON, P. : Theoretical investigation of electrically active defects in silicon. In: *Proceedings 1st ENDEASD Workshop, Santorini, Greece*, 1999, S. 18–30

[14] JUDA, U. ; SCHEERER, O. ; HÖHNE, M. ; RIEMANN, H. ; SCHILLING, H.-J. ; DONECKER, J. ; GERHARDT, A. : Oxygen-related 1-platinum defects in silicon: An electron paramagnetic resonance study. In: *Journal of applied physics* 80 (1996), Nr. 6, S. 3435–3444

[15] KWON, Y. ; ISHIKAWA, T. ; KUWANO, H. : Properties of platinum-associated deep levels in silicon. In: *Journal of applied physics* 61 (1987), Nr. 3, S. 1055–1058

[16] LANG, D. : Deep-level transient spectroscopy: A new method to characterize traps in semiconductors. In: *Journal of applied physics* 45 (1974), Nr. 7, S. 3023–3032

[17] LAUWAERT, J. ; KHELIFI, S. ; VRIELINCK, H. : Determination of majority carrier capture rates via Deep Level Transient Spectroscopy. In: *ECS Journal of Solid State Science and Technology* 5 (2016), Nr. 4, S. P3041–P3047

[18] LØVLIE, L. S.: *Electrical characterization of majority carrier traps in electron irradiated epitaxial N-type Si*, University of Oslo, Diplomarbeit, 2007

[19] LUO, Y.-r. ; KERR, J. : Bond dissociation energies. In: *CRC Handbook of Chemistry and Physics* 89 (2012), S. 89

[20] MANTOVANI, S. ; NAVA, F. ; NOBILI, C. ; CONTI, M. ; PIGNATEL, G. : Thermal diffusion of Pt in silicon from PtSi. In: *Applied Physics Letters* 44 (1984), Nr. 3, S. 328–330

[21] MAZUR, R. ; DICKEY, D. : A spreading resistance technique for resistivity measurements on silicon. In: *Journal of the electrochemical society* 113 (1966), Nr. 3, S. 255–259

[22] MURAKAMI, Y. ; SHINGYOUJI, T. : Separation and analysis of diffusion and generation components of pn junction leakage current in various silicon wafers. In: *Journal of applied physics* 75 (1994), Nr. 7, S. 3548–3552

[23] NIEDERNOSTHEIDE, F.-J. ; SCHULZE, H.-J. ; FELSL, H. ; HILLE, F. ; LAVEN, J. ; PFAFFENLEHNER, M. ; SCHÄFFER, C. ; SCHULZE, H. ; SCHUSTEREDER, W. : Tailoring of field-stop

layers in power devices by hydrogen-related donor formation. In: *Power Semiconductor Devices and ICs (ISPSD), 2016 28th International Symposium on* IEEE, 2016, S. 351–354

[24] PEARTON, S. ; CORBETT, J. ; SHI, T. : Hydrogen in crystalline semiconductors. In: *Applied Physics A* 43 (1987), Nr. 3, S. 153–195

[25] PEARTON, S. ; TAVENDALE, A. : Hydrogen passivation of gold-related deep levels in silicon. In: *Physical review B* 26 (1982), Nr. 12, S. 7105

[26] PONS, D. : Accurate determination of the free carrier capture kinetics of deep traps by space-charge methods. In: *Journal of applied physics* 55 (1984), Nr. 10, S. 3644–3657

[27] SACHSE, J.-U. ; SVEINBJÖRNSSON, E. ; JOST, W. ; WEBER, J. ; LEMKE, H. : Electrical properties of platinum-hydrogen complexes in silicon. In: *Physical Review B* 55 (1997), Nr. 24, S. 16176

[28] SACHSE, J.-U. ; SVEINBJÖRNSSON, E. ; YARYKIN, N. ; WEBER, J. : Similarities in the electrical properties of transition metal–hydrogen complexes in silicon. In: *Materials Science and Engineering: B* 58 (1999), Nr. 1-2, S. 134–140

[29] SCHRODER, D. K.: *Semiconductor material and device characterization.* John Wiley & Sons, 2006

[30] SIMOEN, E. ; CLAEYS, C. ; VANHELLEMONT, J. : Defect analysis in semiconductor materials based on pn junction diode characteristics. In: *Defect and Diffusion Forum* Bd. 261 Trans Tech Publ, 2007, S. 1–24

[31] STESMANS, A. : Dissociation kinetics of hydrogen-passivated P b defects at the (111) S i/S i O 2 interface. In: *Physical Review B* 61 (2000), Nr. 12, S. 8393

[32] SZE, S. M. ; NG, K. K.: *Physics of semiconductor devices.* John wiley & sons, 2006

[33] VON BARDELEBEN, H. ; STIÉVENARD, D. ; BROUSSEAU, M. ; BARRAU, J. : EPR observation of a platinum pair complex in Si. In: *Physical Review B* 38 (1988), Nr. 9, S. 6308

[34] WEISS, S. : *Halbleiteruntersuchungen mit dem DLTFS-(deep-level transient fourier spectroscopy-) Verfahren*, Gesamthochschule Kassel, Diss., 1991

[35] ZOHTA, Y. ; OHMURA, Y. ; KANAZAWA, M. : Shallow donor state produced by proton bombardment of silicon. In: *Japanese Journal of Applied Physics* 10 (1971), Nr. 4, S. 532

[36] ZYLBERSZTEJN, A. : Trap depth and electron capture cross section determination by trap refilling experiments in Schottky diodes. In: *Applied Physics Letters* 33 (1978), Nr. 2, S. 200–202